LITHOS 512-513 (2025) 108155

Contents lists available at ScienceDirect

LITHOS

journal homepage: www.elsevier.com/locate/lithos

Petrogenetic processes in alkaline magmatism in the southern Mozambique Channel

C. Berthod [a,b,c,*], P. Bachèlery [c], S. Revillon [d,e], R. Doucelance [c], F. Schiavi [c], J.-L. Devidal [c], E. Bou [c], S.J. Jorry [e]

[a] Observatoire Volcanologique et Sismologique de la Guadeloupe, Institut de physique du globe de Paris, 97113 Gourbeyre, France
[b] Université Paris Cité, Institut de Physique du Globe de Paris, CNRS, 75005 Paris, France
[c] Université Clermont Auvergne, CNRS, IRD, OPGC, Laboratoire Magmas et Volcans, 6 avenue Blaise Pascal, 63178 Aubière, France
[d] SEDISOR, 65 place N. Copernic, Plouzané, France
[e] GEO-OCEAN, Univ. Brest-CNRS-Ifremer, UMR 6538, 29280 Plouzané, France

ARTICLE INFO

Keywords:
Mozambique Channel
Volcanism
Seamounts
Petrology
Europa and Bassas da India

ABSTRACT

Whereas the northern part of the Mozambique Channel, between the eastern coast of Africa and Madagascar, is intensively studied, the southern part remains poorly investigated. The 2014 PAMELA-MOZ01 and 2015 PAMELA-MOZ04 cruises enabled us to collect volcanic rocks from the submarine flanks of the Bassas da India-Europa complex, including Bassas da India atoll, Europa Island, and Jaguar and Hall Banks. Despite significant alteration, probably due to their prolonged stay in seawater and the hydrothermal circulation they underwent, we are able to describe the main petrological and geochemical aspects of these largely unknown lavas. To achieve this, we integrated petrographic and mineralogical observations with geochemical analyses of the dredged rocks, aiming to identify the key aspects of the alteration and to characterize their petrological and geochemical properties.

The volcanism of this region is characterized by strongly silica-undersaturated alkaline magmas. Here, we demonstrate that this volcanism is marked by a bimodal magmatic activity with ultrabasic and basic compositions, and more silica-rich compositions. Using isotopic signatures and trace elements, we suggest that magmas are produced by a low degree of partial melting (1 to 5 %) of a metasomatized mantle at about 80 km depth. These mafic magmas then rise from the source to the surface via several magma storage levels, located at about 25–30 km and 15 km depth, the latter corresponding to the mantle-crust boundary as identified by geophysical methods. Fragments of zoned sanidine phenocrysts within intermediate lavas (olivine-free nephelinite or tephriphonolite) also suggest the presence of differentiated magma reservoirs. Our observations strongly support frequent magmatic recharges, coupled with magma differentiation through olivine + clinopyroxene crystallization/assimilation, in long-lived magma reservoirs. In many respects, this volcanism has similar characteristics (nature of the source, degree of partial melting, composition of the lavas, age, and spatial distribution) to those of the Miocene to Quaternary volcanic provinces of Madagascar, the northern Mozambique Channel or the East African Rift. We propose that this volcanism might result from regional extension through the Mozambique Channel and the southern part of the East African Rift System, coupled with a thermal erosion of a mantle plume.

1. Introduction

The Mozambique Channel is characterized by a long-lived magmatic activity from c. 180 Ma to the present (e.g., Mueller and Jokat, 2017; Roche and Ringenbach, 2022; Senkans et al., 2019; Watremez et al., 2021), expressed as scattered volcanic islands and seamounts. They include, from north to south, the Glorieuses and Comoros Archipelagos, the Sakalaves seamounts (Davie Ridge), Juan de Nova Island, Bassas da India-Europa complex, and Almirante Leite (Fig. 1). Bassas da India and Europa are located in the southwestern Mozambique Channel at 21.5°S – 39.5°E and 22.3° S – 40.3° E, respectively. Recent oceanographic acquisitions (bathymetric surveys, dredging, and seismic profiles, Jorry, 2014; Olu, 2014; Jouet and Deville, 2015) have revealed flat-topped seamounts currently drowned at hundreds of meters deep, e.g., Hall

* Corresponding author at: Observatoire Volcanologique et Sismologique de la Guadeloupe, Institut de physique du globe de Paris, 97113 Gourbeyre, France.
E-mail address: berthod@ipgp.fr (C. Berthod).

https://doi.org/10.1016/j.lithos.2025.108155
Received 30 January 2025; Received in revised form 6 June 2025; Accepted 7 June 2025
Available online 19 June 2025

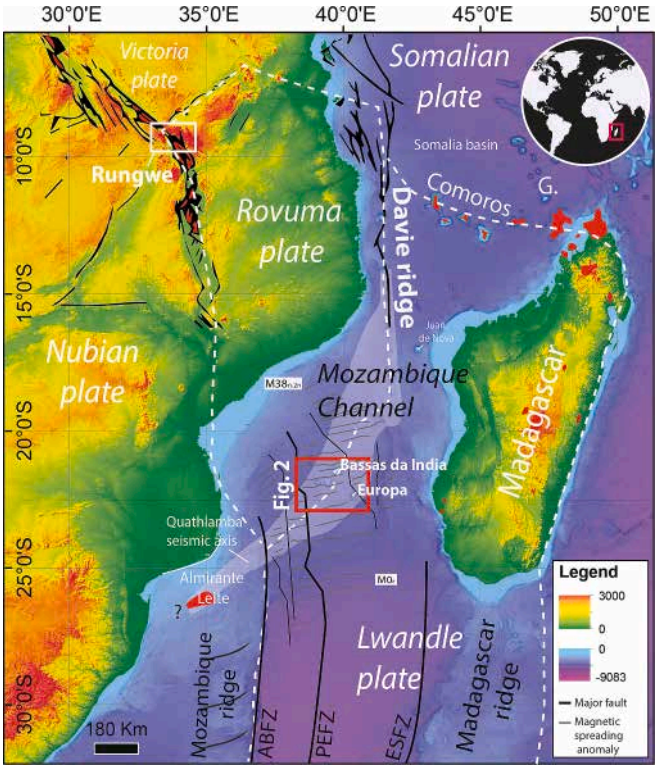

Fig. 1. Geological context showing the study area (red box) located on the Quathlamba seismic axis, GEBCO 30 arc-second global grid of elevation 2014, about 930 m-resolution after Berthod et al. (2022a). White hatched lines: proposed plate boundaries, Neogene-to-present volcanism: red areas, G: Glorieuses, ABFZ: Andrew Bain Fracture Zone, PEFZ: Prince Edward Fracture Zone, ESFZ: Eric Simpson Fracture Zone. (For interpretation of the references to colour in this figure legend, the reader is referred to the web version of this article.)

and Jaguar Banks, SW of Bassas da India, and Ptolemee seamount, SE of Bassas da India (Fig. 2). These volcanic highs, located along the Quathlamba Seismic Axis (Saria et al., 2014), are poorly known. First work was recently performed by Courgeon et al. (2016), Courgeon et al. (2017), and Counts et al. (2018), focusing on the carbonate platforms and associated shallow volcanic structures of this complex. Lately, Berthod et al. (2022a) imaged the regional distribution and the morphology of the volcanic structures, using multibeam bathymetry and acoustic backscatter images around Bassas da India, Europa, and the surrounding edifices, acquired during the PAMELA-MOZ01 (Olu, 2014) and PAMELA-MOZ04 (Jouet and Deville, 2015) cruises. These authors confirm the volcanic nature of the Bassas da India-Europa complex. They highlight a clear tectonic control in the formation of the submarine seamounts and underline the relevance of considering Cenozoic volcanism in the geodynamic evolution of the Mozambique Channel.

The origin of the Cenozoic volcanism of the southern Mozambique Channel is still open to debate. Based on geodynamic studies, two hypotheses have been proposed: (1) Bassas da India and the surrounding volcanic structures could belong to a chain of volcanic seamounts (Almirante Leite – Eggert Seamount – Bassas group) related to the Lesotho-Natal mantle hotspot (Gilfillan et al., 2019; Hartnady, 1985). Using this hotspot theory, coupled with the African absolute motion, Hartnady (1985) proposed an age of about 50–55 Ma for the Bassas da India-Europa volcanism; (2) Volcanism could result from lithospheric thinning and mantle uplift, which could lead to partial melting, with, according to some authors, the possible influence of a deep mantle superplume (O'Connor et al., 2019). Indeed, the volcanism of the SW Mozambique Channel is mainly constrained by the complex tectonic history, with three blocks between the Nubia and Somalia plates, known as the Victoria, Rovuma and Lwandle blocks (Michon et al., 2022; Saria et al., 2014; Wiles et al., 2020). Therefore, Courgeon et al. (2016), Courgeon et al. (2017), and Deville et al. (2018) propose that the eastern branch of the East African Rift System (EARS) extends much further south than previously postulated. Based on the contemporaneity of volcanism and extensive tectonics, Michon et al. (2022) proposed the structures and volcanism of the Mozambique Channel form the southern part of the EARS, with a link between "an overall complex mantle upwelling dynamics" and the "extensive stresses acting on the African lithosphere".

This paper provides the first petrological and geochemical description and analysis of the volcanic formations in the Bassas da India atoll and Europa Island region, based on rock samples dredged during the PAMELA-MOZ01 and PAMELA-MOZ04 cruises (Jouet and Deville, 2015; Olu, 2014). We combined for this purpose petrographic and mineralogical observations with geochemical analyses. We determine the nature and origin of these volcanic edifices, and we image their magmatic system.

2. Geological context

The Mozambique Channel is located in the southwest Indian Ocean, between the African continent and Madagascar (Fig. 1). The opening of the Mozambique Channel is related to both the Gondwana breakup, which occurred during the Early Jurassic-Early Cretaceous time interval (Mueller and Jokat, 2019; Roche et al., 2022; Roche and Ringenbach, 2022; and references therein), and to the southward shift of "Antarctico-Indio-Madagascarian" continental block relative to Africa (~165–120 Ma, Mueller and Jokat, 2019, and references therein), due to the activity of a major NNW-SSE transform fault known as the "Davie Ridge" (Fig. 1, Vormann and Jokat, 2021, and references therein). This transform fault divides the Mozambique Channel into two basins, Somalia basin to the north and Mozambique Channel to the south.

Beyond the mere idea that the Mozambique Channel may be affected by extensional tectonic deformation linked to the diffuse southern extension of the East African Rift System (e.g., Kusky et al., 2010), recent studies, notably based on GPS measurements and seismology (Michon et al., 2022 and references therein), have proposed new kinematic models that take into account the existence and contribution of three microplates (Victoria, Rovuma, and Lwandle), in addition to the major Nubian and Somalian plates (Fig. 1). Although the exact boundaries between these microplates are still debated (Thinon et al., 2022), authors tend to agree in considering that the southern Mozambique Channel is crossed, from NE to SW, by the Rovuma-Lwandle plate boundary, following the Quathlamba seismic axis (Michon et al., 2022).

Two shallow-water carbonate platforms, three seamounts, and two coral-capped atolls form the Bassas da India-Europa volcanic complex in the southern Mozambique Channel. From south-west to north-east, these are Hall Bank, Jaguar Bank, and Bassas da India atoll, while four additional edifices, Ptolemee seamount, Pamela Seamounts 1 and 2, and Europa Island (Fig. 2), define a SE-NW alignment with Bassas da India (Berthod et al., 2022a). More than 430 submarine volcanic cones have been identified from a high-resolution statistical study, located on, around and between the large edifices (Berthod et al., 2022a). This volcanism is located along the presumed Rovuma-Lwandle boundary (Fig. 1). Analysis of the spatial distribution of active faults performed by Deville et al. (2018) reveals the presence of a 200 km-wide system of faults, trending N45–80°, with a second set trending N160–180° (Fig. 2). According to Courgeon et al. (2016, 2017) and Berthod et al. (2022a), these faults are clearly associated with volcanic features, suggesting that magma ascent is strongly controlled by large preexisting crustal structures. Berthod et al. (2022a), based on their investigation of volcanic morphologies, propose that some of the large volcanic edifices are connected by volcanic ridges (Fig. 2). They suggest that the morphology of the volcanic ridges is consistent with the existence of shallow magma storage zones, allowing magma to intrude laterally into the rift zones to

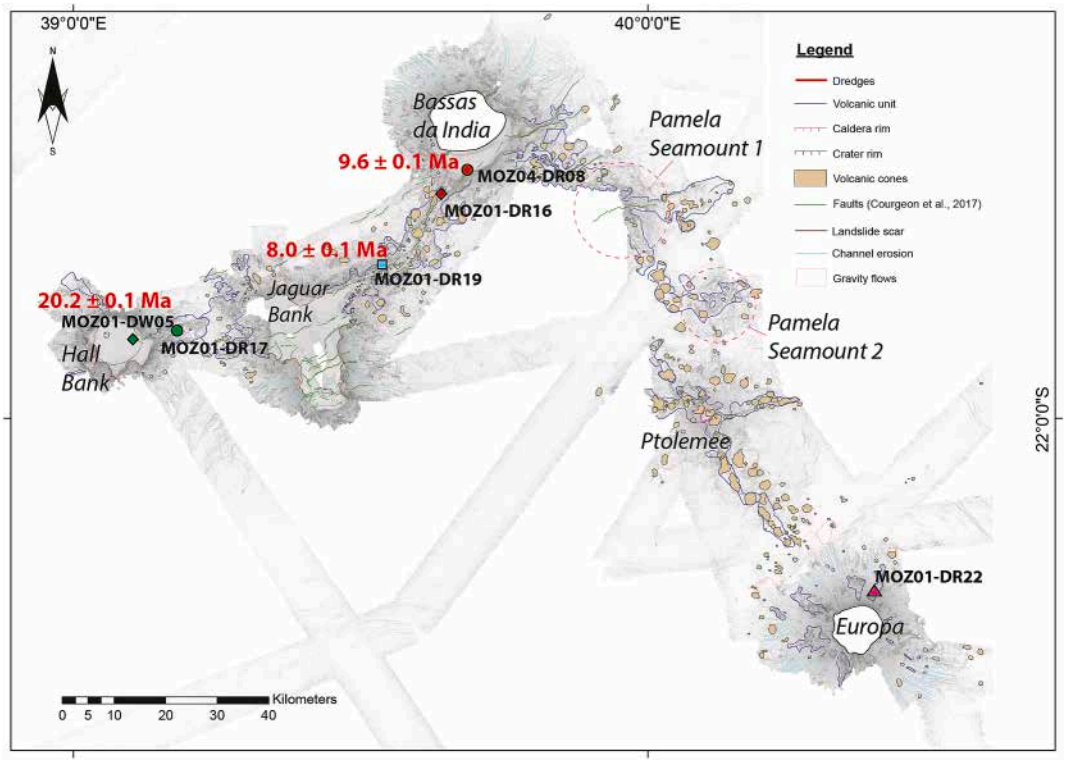

Fig. 2. Bathymetry and dredge positions around islands and seamounts. The known isotopic ages of some volcanic samples are shown in red (after Berthod et al., 2022a). (For interpretation of the references to colour in this figure legend, the reader is referred to the web version of this article.)

feed fissure eruptions, and building small volcanic cones and lava flows. In contrast, they suggest that the large volcanic cones are more likely the result of sporadic subvertical ascent of magma from a deep reservoir located in the mantle or at the base of the crust, bypassing more superficial storage areas.

Based on the interpretation of seismic data across Bassas da India and Europa, Raillard (1990) proposed a volcanic activity in this region since the early Eocene (~55 Ma). More recently, the Hall Bank drowned carbonate platform has been dated using strontium isotopic stratigraphy, giving a minimum age of 16.2 Ma for the Hall Bank substratum (Courgeon et al., 2016). In addition, the first $^{40}Ar/^{39}Ar$ dates for volcanic samples dredged from this region (Berthod et al., 2022a) have revealed that the volcanism covers a period from the Oligo-Miocene to the Pleistocene (8–20.2 Ma, Fig. 2), and probably extends to the present day.

Table 1
Location of dredges and samples collected during 2014 PAMELA-MOZ01 and PAMELA-MOZ04 cruises (Jouet and Deville, 2015; Olu, 2014).

Location	Cruise	DOI	Dredge	Latitude start	Longitude start	Depth start (m)	Latitude end	Longitude end	Depth end (m)	Samples
Bassas da India	*MOZ01*	*10.17600/14001000*	*DR16*	S 21°36.6496'	E 39°38.4227'	1646	S 21°36.4230'	E 39°38.2166'	1332	*DR16a* *DR16b* *DR16–02* *DR16–03* *DR16–05* *DR16–07* *DR16–09*
Bassas da India	*MOZ04*	*10.17600/15000700*	*DR08*	*S 21°34.2483'*	*E 39°40.5783'*	*521*	*S 21°34.7'*	*E 39°40.59'*	*520*	*DR08* *DR08–C1* *DR08–C2*
Hall Bank	*MOZ01*	*10.17600/14001000*	*DR17*	S 21°51.1472'	E 39°10.9124'	1901	S 21°50.42'	E 39°11.0118'	1845	*DR17–02* *DR17–05*
Hall Bank	*MOZ01*	*10.17600/14001000*	*DW05*	S 21°51.3409'	E 39°6.1522'	512	S 21°51.8028'	E 39°6.3817'	507	*DW05–03* *DW05–03S* *DW05–04* *DW05–06* *DW05–07* *DW05–13*
Jaguar Bank	*MOZ01*	*10.17600/14001000*	*DR19*	S 21°43.6855'	E 39°32.3300'	1313	S 21°44.1027'	E 39°32.3016'	990	*DR19–03* *DR19–04* *DR19–06*
Europa	*MOZ01*	*10.17600/14001000*	*DR22*	S 22°17.9541'	E 40°23.7225'	1554	S 22°18.1297'	E 40°23.4781'	1320	*DR22–04* *DR22–05* *DR22–06* *DR22–07*

3. Samples and methods

Our study was realized on volcanic rocks dredged during 2014 PAMELA-MOZ01 and 2015 PAMELA-MOZ04 cruises (Olu, 2014; Jouet and Deville, 2015, Table 1). MOZ01-DW05 and MOZ01-DR17 dredges have been performed on Hall Bank. MOZ01-DR19, MOZ01-DR16 - MOZ04-DR08, and MOZ01-DR22 have been collected on Jaguar Bank, Bassas da India and Europa submarine slopes, respectively (Fig. 2). The six dredges totalize 25 samples (Table 1) that allow us to define the petrographic characteristics of the volcanic rocks.

Mineral phases were identified at Laboratoire Magmas et Volcans (LMV, Clermont-Ferrand, France) using a Renishaw inVia confocal Raman micro-spectrometer and CAMECA SX-100 and CAMECA SX Five Tactis electron microprobes. Bulk-rock concentrations and isotopic compositions have been obtained by ICP-AES, ICP-MS, TIMS and MC-ICP-MS at LMV and LGO (PSO/IUEM, Plouzané, France). Each method is described in supplementary material.

4. Results

4.1. Petrography and classification

As geochemical criteria can only be used to a limited extent due to the degree of alteration or the small size of many samples, our classification is firstly based on the mineral paragenesis of the rocks. Additional considerations will be made, if necessary, when examining the chemical compositions. Following Cucciniello et al. (2023), basanites are distinguished from nephelinites by the presence of modal plagioclase, while nephelinites may contain Ba-rich mica and Ba-rich sanidine in the groundmass, but no plagioclase. Most of the dredged samples

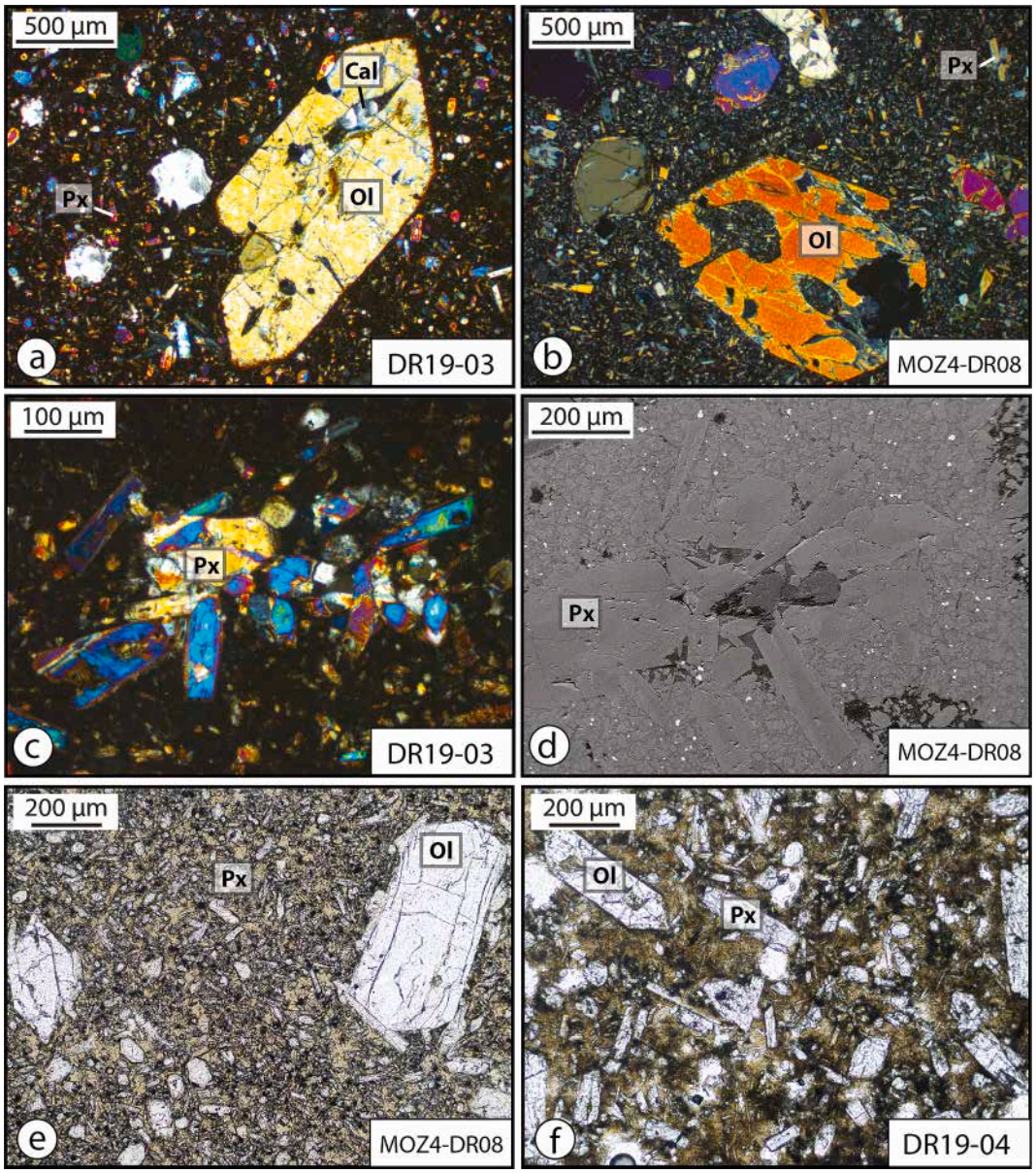

Fig. 3. Representative transmitted-light microphotographs with crossed polars and BSE images of melanocratic to holomelanocratic nephelinites collected on the flank of Jaguar Bank (MOZ01-DR19–03 and MOZ01-DR19–04) and Bassas da India (MOZ04-DR08). a) MOZ01-DR19–03 and b) MOZ04-DR08 samples display a porphyritic texture, and contain euhedral to sub-euhedral clinopyroxene and olivine phenocrysts. c-d) The groundmass is mainly composed of clinopyroxene microlites with irregular normal zoning, nepheline, and oxides. Clinopyroxene microlites can form clusters and may be altered to amphibole. e-f) Unaltered (MOZ04-DR08) or palagonitized (MOZ01-DR19–04) vitreous matrix providing clear confirmation of the absence of plagioclase crystal. Ol: olivine, Px: clinopyroxene, Cal: calcite.

mineralogically correspond to melanocratic to holomelanocratic nephelinites and basanites. Some facies collected on the Hall Bank carbonate platform (Courgeon et al., 2016), with phenocrysts of alkali feldspar, and in some cases nepheline phenocrysts, are considered to be more evolved lavas potentially ranging from intermediate nephelinite to phono-tephrite or tephri-phonolite.

4.2. Mafic lavas

Samples dredged on the flanks of Jaguar Bank (MOZ01-DR19–03, MOZ01-DR19–04, and MOZ01-DR19–06) and of Bassas da India atoll (MOZ04-DR08) are highly porphyritic rocks composed of sub-euhedral to euhedral olivine (< 1 cm), clinopyroxene, Cr-spinel, and Fe—Ti oxide phenocrysts embedded in a clinopyroxene-rich matrix with nepheline, Fe—Ti oxides, Cr-spinel, biotite, and apatite (< 500 μm, Fig. 3a, b). A glassy phase can sometimes be observed in the matrix of some samples. Although olivine megacrysts are mainly euhedral, many of them are spongy crystals, with large embayments, and spherical to ovoid pockets containing matrix material (including euhedral clinopyroxene microcrysts, and chrome spinel) and frequently calcite (Fig. 3a, b). Calcite (± fibrous zeolites) also fills the vesicles and fractures of the rock. Spongy olivine crystals are interpreted as evidence of initial rapid growth, rather than partial dissolution (Welsch et al., 2014). Clinopyroxene crystals display a large range of size from <10 μm to ~500 μm, and are observed as clusters (Fig. 3c, d). Some olivine and clinopyroxene show intergrown crystals, with irregular and intricate boundaries. Clinopyroxene crystals are generally unaltered, with the exception of a few crystals altered to amphibole. They show irregular normal zoning (Fig. 3c, d) suggesting the influence of fluids, and/or a complex history of magma recharge and mixing. These lavas contain no visible plagioclase and can therefore be considered as nephelinites. A few samples with an unaltered (MOZ04-DR08) or palagonitized

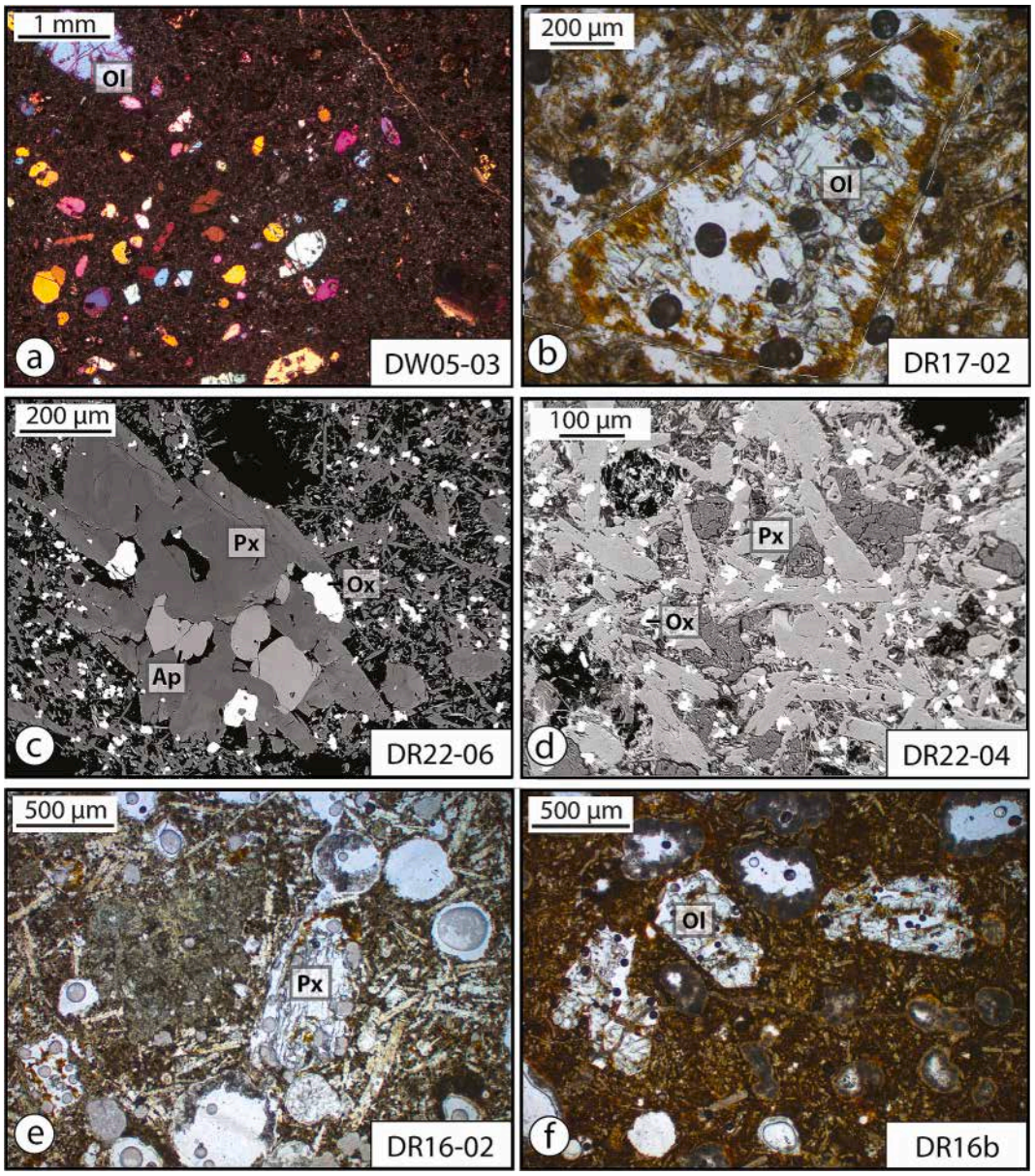

Fig. 4. Representative microphotographs and BSE images of volcanic samples collected in the southern part of the Mozambique Channel. a) Olivine phenocrysts in an aphanitic groundmass in olivine basanite MOZ01-DW05–03 sample from Hall Bank. b) Altered olivine with an iddingsite border in MOZ01-DR17–02 sample from Hall Bank. c) Complex zoning in clinopyroxene crystal aggregated with oxide and apatite (MOZ01-DR22–06). d) Well-developed microlites observed in the MOZ01-DR22–04 sample. Olivine basanites e) MOZ01-DR16–02, and f) MOZ01-DR16b dredged on the flank of Bassas da India. Ol: olivine, Px: clinopyroxene, Ox: oxide, and Ap: apatite.

(MOZ01-DR19–04) vitreous matrix provide clear confirmation of the absence of plagioclase crystal, and the only presence of clinopyroxene and olivine microlites or microcrystals (Fig. 3e, f), indicating the "ultramafic" character of these lavas, in agreement with the high forsterite content (up to Fo88) of olivine in equilibrium (Table S1 in supplementary material). These rocks are petrographically very similar to the "ankaratrites" described among the Cenozoic lavas of Madagascar (e.g., Cucciniello et al., 2023; Melluso et al., 2011).

Samples collected at the top (MOZ01-DW05–03) and west of Hall Bank (MOZ01-DR17–02, MOZ01-DR17–05) are sub-aphyric to porphyritic. They contain olivine phenocrysts, sometimes millimeter-sized, mostly altered to iddingsite and calcite, as well as Cr-rich spinels (Fig. 4a-b). The groundmass is always very rich in clinopyroxene microcrystals and microlites, with olivine, nepheline, and Fe—Ti oxides. Other mineral phases such as biotite, perovskite, and apatite (< 100 μm) have also been identified in the groundmass of MOZ01-DW05–03 (Table 1 and Fig. 4). The presence of perovskite in this sample is a further sign of the primitive nature of these lavas. However, alkali feldspar and plagioclase microlites (andesine) were identified in the groundmass of sample MOZ01-DR17–05. MOZ01-DR17–05 can therefore be classified as an olivine basanite.

Olivine is also the main macrocrystalline phase (sometimes accompanied by a few clinopyroxenes and Fe—Ti oxides) in the samples collected on the submarine flanks of Europa Island (MOZ01-DR22–04, MOZ01-DR22–05, MOZ01-DR22–06, and MOZ01-DR22–07, Fig. 4c-d). Due to the strong alteration of these rocks, olivine phenocrystals usually appear as a ghost phase, highlighted by an iddingsite border. When present, clinopyroxene crystals show complex zoning, sometimes with a sieve-textured core, or intergrowth with apatite and oxide crystals (Fig. 4c).

Lavas sampled on the south volcanic ridge of Bassas da India atoll (MOZ01-DR16a, MOZ01-DR16b, MOZ01-DR16–02, MOZ01-DR16–03, MOZ01-DR16–05, MOZ01-DR16–07) are moderately to strongly porphyritic, with olivine and sometimes clinopyroxene as main macrocrystalline phases. These samples usually contain large euhedral to subeuhedral olivine phenocrysts (50 μm – 1 mm, Fig. 4e-f) with sparse chrome spinel inclusions, occasionally exhibiting kink-band structures. In several samples (MOZ01-DR16a, MOZ01-DR16–02, MOZ01-DR16–03, MOZ01-DR16–05, MOZ01-DR16–07), a ghost mineral was found, pseudomorphically replaced by a crystalline mixture probably containing hydroxides and amorphous materials. This mineral formed elongated crystals a few hundred μm in length (Fig. 4e). It was not possible to identify it formally.

In the mafic rocks from Bassas da India, Europa and Hall Bank, microlites in the groundmass mesostasis present variable development. Most often, the rocks are characterized by well-developed elongated microcrystals and microlites (up to 500 μm) of clinopyroxene (e.g., in the MOZ01-DR16 and MOZ01-DR22 samples, Fig. 4), which may be accompanied by Fe—Ti oxides, chrome spinel, nepheline, haüyne, biotite, apatite, and few plagioclase crystals. Zeolites and calcite are sometimes found as a secondary phase in vesicles.

4.3. Intermediate lavas

MOZ01-DW05–13, MOZ01-DW05–04, MOZ01-DW05–06, MOZ01-DW05–08, and MOZ01-DW05–09 samples, collected as scattered pebbles at the top of the Hall Bank, have a moderately porphyritic texture, with phenocrysts set in a fine-grained microcrystalline mesostasis. Their mineralogical composition and texture suggest that these samples could be olivine-free nephelinite or tephri-phonolite. In MOZ01-DW05–13 and MOZ01-DW05–06 samples, the mineral assemblage includes alkali feldspar, nepheline, clinopyroxene, biotite, titanite, amphibole, Fe—Ti

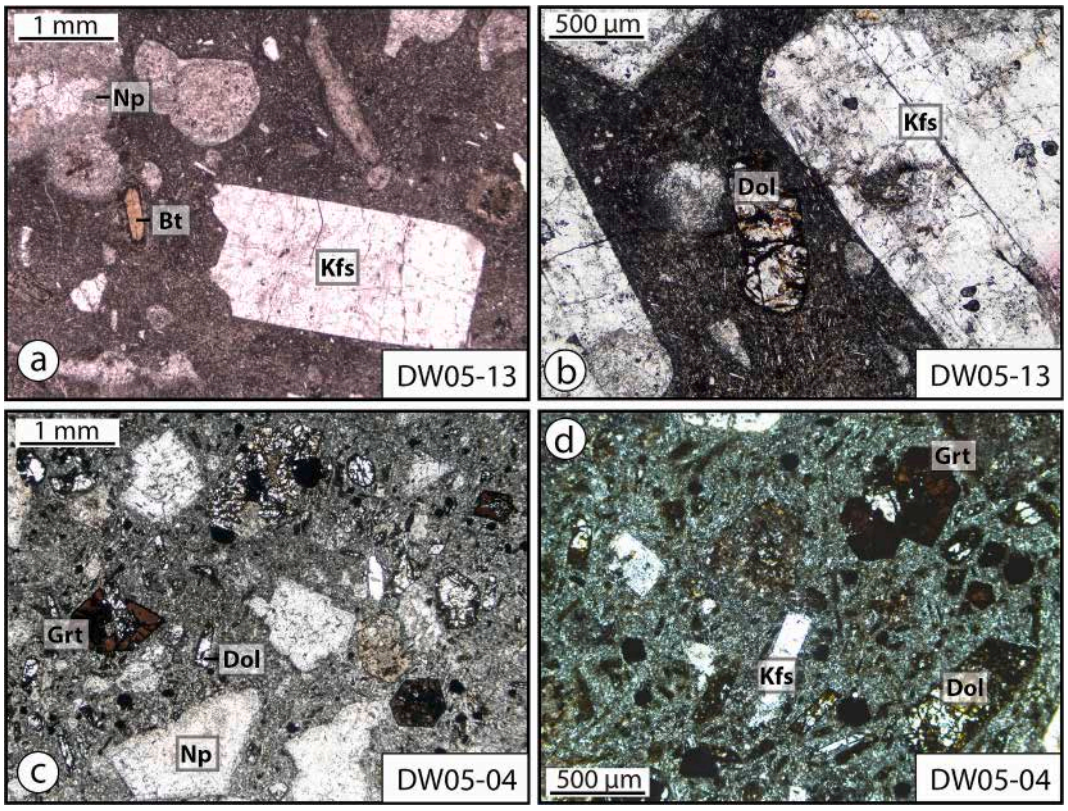

Fig. 5. a) Alkali feldspar and nepheline phenocrysts, and destabilized biotite crystal in MOZ01-DW05–13 Hall sample. b) Sud-euhedral dolomite crystal observed in the groundmass of MOZ01-DW05–13 sample. c-d) Euhedral to sub-euhedral biotite, dolomite, nepheline, sanidine, and Ti-rich garnet crystals in a microcrystalline groundmass of sanidine, biotite and Fe—Ti oxides in the DW05–04 sample. Ol: olivine, Ox: oxide, Bt: biotite, Np: nepheline, Kfs: alkali feldspar, Dol: dolomite, Grt: Ti-rich garnet (schorlomite).

oxides, and dolomite. Alkali feldspar is the dominant phenocrystal phase and occurs as large euhedral to sub-euhedral crystals (0.5 mm – 4 cm, Fig. 5a-b). It is worth noting that alkali feldspar is often seen as crystal fragments and exhibits complex zoning with resorbed core and non-systematic zoning (Fig. 6a). Biotite occurs as zoned sub-euhedral to anhedral corroded crystals (< 1 mm, Figs. 5a and 6b). Biotite antecrystals contain apatite and titanite inclusions. Groundmass is composed of numerous microlites of <200 μm elongated alkali feldspar, nepheline, apatite, and Fe—Ti oxides. Importantly, few dolomite crystals have been found in the groundmass (Fig. 5b-d).

MOZ01-DW05–04, MOZ01-DW05–08, and MOZ01-DW05–09 display a slightly different paragenesis. These samples are characterized by a porphyritic texture with strongly altered microcrystalline groundmass of sanidine, biotite, and Fe—Ti oxides. Phenocrysts are mainly euhedral and zoned. They consist of alkali feldspar, dolomite, biotite, and amphibole. Smaller phenocrysts are titanite and Ti-rich garnet (schorlomite, Fig. 5c-d). Some alkali feldspar phenocrysts contain inclusions of titanite and magnetite. Calcite and albite have been recognized in the microlitic groundmass.

4.4. Magmatic phase chemistry

Individual analyses (around 1000 analyses) were obtained on the mineral chemistry of the volcanic rocks of the Bassas da India-Europa volcanic provinces. A selection for each mineral phase is reported in supplementary data, Tables S1-S6.

4.4.1. Olivine

In most cases, olivine is the dominant phenocryst phase in our samples, with sub-euhedral to euhedral crystal shapes. Bassas da India samples contain Mg-rich olivine crystals, with compositions ranging from Fo85 to Fo89 (Mg/(Mg + Fe)*100, Fig. 7a and Table S1 in supplementary material). In these samples, olivine crystals are also sporadically found as microlites in the groundmass with compositions varying from Fo87 to Fo89. Thus, no correlation was observed between size, composition, and textural position (phenocryst vs. microlite). Olivine phenocrysts in Europa samples are clustered with Fo and MnO content ranging from 82 to 83 and from 0.17 to 0.28 wt.%, respectively. This cluster may be due to the limited number of analyses (n = 17, Fig. 7b). No microlite was observed in the samples from Europa. In contrast, phenocrysts and microlites of olivine in Hall Bank samples have a much more dispersed composition, with Fo and MnO contents varying from 74.4 to 89.0 and 0.13 to 0.78 wt.%, respectively. Finally, olivine phenocrysts and microlite in Jaguar Bank samples are similar in composition to Bassas da India atoll, with Fo ranging from 81.4 to 88.3 and MnO content varying between 0.12 and 0.47 wt.% (Fig. 7b).

4.4.2. Clinopyroxene

Clinopyroxene is a very common phase, particularly in the most mafic lavas. Clinopyroxene is mainly diopside ($Wo_{23–45}$ $En_{43–55}$ $Fs_{7–23}$) found both as phenocrysts and microlites in the groundmass. Mg numbers (Mg# = molar Mg/(Mg + Fe)*100) are more scattered than the Fo content of olivine crystals, and range from 47.4 to 87.9 (Fig. 7c and Table S2 in supplementary material). Except for Bassas da India atoll, clinopyroxene phenocrysts (Mg# ranging from 59.3 to 87.9) tend to have a more primitive composition than microlites (51.0–83.9, respectively). However, the compositional variations differ from one site to another.

Regarding Bassas da India, clinopyroxene phenocrysts and microlites have a similar composition in sample MOZ01-DR16a, with a Mg# at 58.2–80.4, TiO_2 contents at 2.0–9.4 wt.% and Al_2O_3 contents ranging from 5.76 to 13.9 wt.% (Fig. 7c, d), whereas the clinopyroxene phenocrysts show more primitive compositions (Mg# at 72.7–84.4, TiO_2 contents at 1.5–4.5 wt.%, and Al_2O_3 contents at 3.7–9.8 wt.%) than the microlites in samples MOZ01-DR16b and MOZ04-DR08 (Mg# = 58.8–82.1, TiO_2 = 2.1–6.7 wt.%, and Al_2O_3 = 5.2–12.1 wt.%). Finally, in MOZ01-DR16–07 sample, phenocrysts show more evolved composition with a Mg# ranging from 58.1 to 60.9, TiO_2 contents at 2.5–5.9 wt.%, and Al_2O_3 contents at 10.1–12.6 wt.%.

On Europa, MOZ01-DR22–06 sample contains phenocrysts and microlites of clinopyroxene. Phenocrysts display Mg# varying from 67.0 to 87.9 (TiO_2 = 0.4–5.4 wt.%, and Al_2O_3 = 0.5–10.7 wt.%), which tends to be more primitive than Mg# = 61.1–77.9 microlites (TiO_2 = 2.3–7.0 wt.%, and Al_2O_3 = 4.0–11.8 wt.%). Phenocrysts in this sample show a complex zoning and intergrowth with inclusions of apatite and Fe—Ti oxides. In MOZ01-DR22–04 and MOZ01-DR22–05 samples,

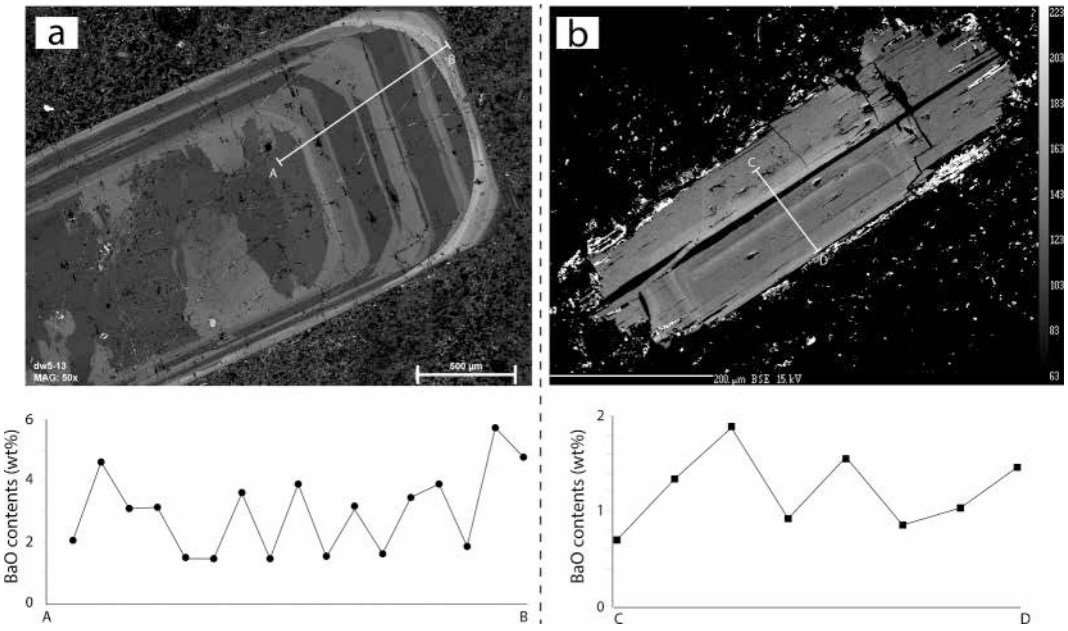

Fig. 6. BSE images and associated BaO (wt%) profiles in representative zoned alkali feldspar phenocrysts (a) and biotite antecrysts (b) from Hall Bank (MOZ01-DW05–13 sample). Brightness reflects elevated Ba concentrations. Note dark, partially resorbed, cores in the alkali feldspar phenocryst and variably complex zoning in overgrowth.

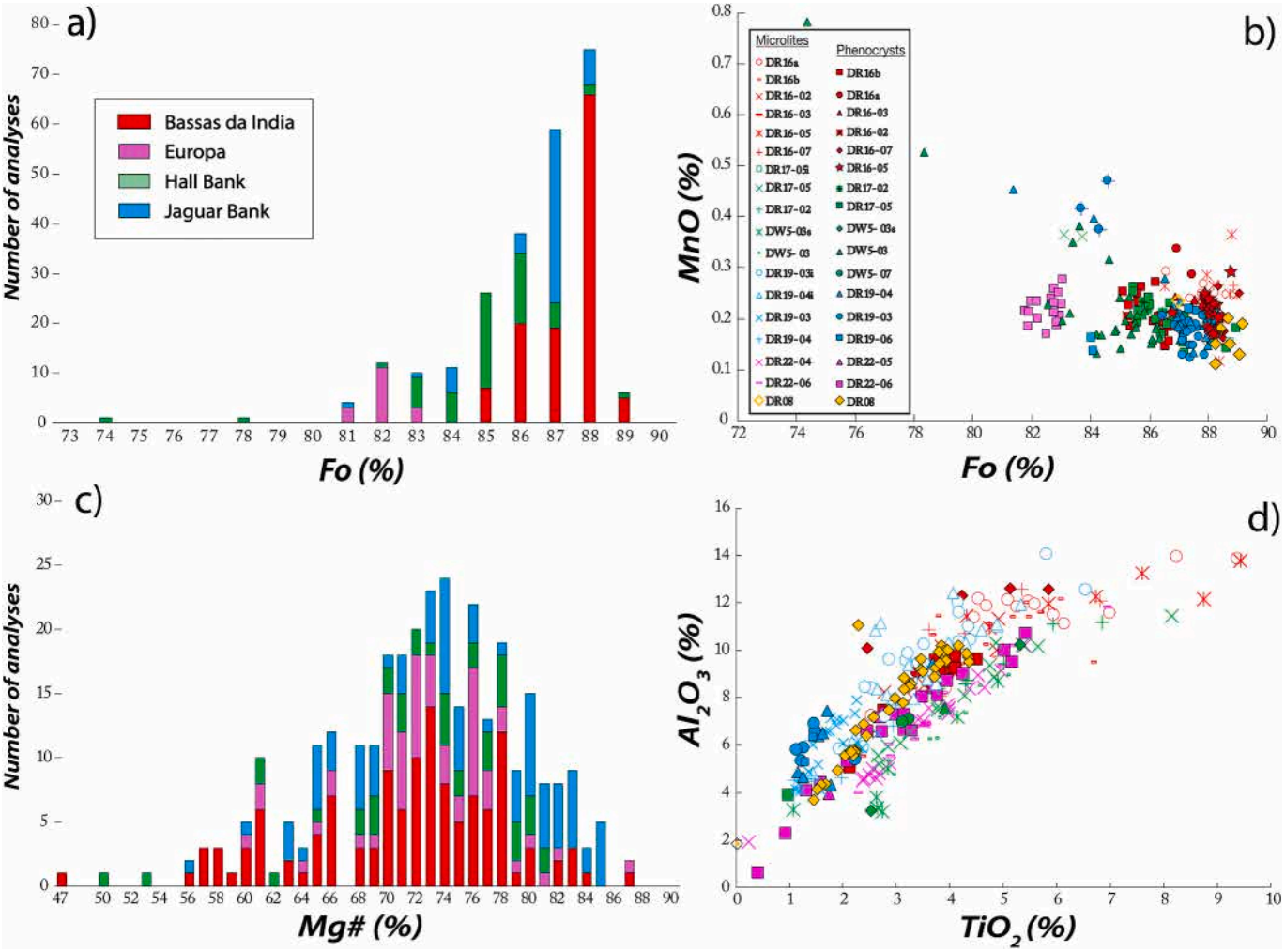

Fig. 7. Composition of olivine (a, b) and clinopyroxene (c, d) in the Bassas da India-Europa volcanic rocks.

clinopyroxene microlites present Mg#, TiO_2, and Al_2O_3 ranging from 62.8 to 78.2, 0.2–7.2 wt.% and 1.9–10.6 wt.%, respectively.

In Hall Bank samples, clinopyroxene crystals present Mg# varying between 51 and 81.7, TiO_2 contents at 1.0–8.2 wt.% and Al_2O_3 contents at 3.2–11.4 wt.%. Clinopyroxene in Jaguar samples, that correspond to the more mafic rocks, displays the most primitive composition of all studied samples, with a Mg# ranging from 57.2 to 85.4 (Fig. 7c, d). TiO_2 and Al_2O_3 contents vary from 1.1 to 6.6 wt.% and 4.0 to 14.0 wt.%, respectively.

4.4.3. Feldspars and feldspathoids

Feldspar crystals from Bassas da India and Europa samples could not be analyzed due to their strong alteration. Feldspars in Hall Bank samples present scattered composition. MOZ01-DR17–05 sample contains andesine (phenocrysts and microlites) with a composition at $An_{33–34}$ $Ab_{62–64}$ $Or_{3–5}$, Al_2O_3 and Na_2O contents ranging from 24.8 to 25.2 wt.% and from 6.7 to 7.1 wt.%, respectively (Fig. 8a, b). On Hall bank, feldspar crystals were analyzed (MOZ01-DW05–04, MOZ01-DW05–06, and MOZ01-DW05–13, Fig. 5b-d), with variable compositions at $An_{0–11}$ $Ab_{19–53}$ $Or_{47–79}$, 17.9–21.5 wt.% Al_2O_3 and 2.2–7.2 wt.% Na_2O. They mainly are sanidine, observed as phenocrysts and microlites in the groundmass (Fig. 5b). Sanidine phenocrysts are characterized by zoning patterns. Compositional profiles reveal an important variation in BaO contents through the crystals (Fig. 6a). In fact, BaO contents range from 0.1 to 5.8 wt.% in samples in which BaO was analyzed (MOZ01-DW05–06 and MOZ01-DW05–13). Nepheline crystals, in the MOZ01-DW05–03 and MOZ01-DW05–03s samples, are characterized by Al_2O_3 and Na_2O contents ranging from 32.7 to 34.9 wt.% and from 12.7 to 14.5 wt.%, respectively (Fig. 8b).

4.4.4. Oxides

Fe—Ti oxides crystals were observed in all samples mainly as a groundmass phase (Figs. 4, 5 and 6). They are chrome spinels, ilmenites and titanomagnetites (Fig. 8c, d). Numerous chrome spinels were observed as inclusion in olivine crystals, which is consistent with the primitive olivine composition (Fo ranging from 74.4 to 89.1, Fig. 7a, b), whereas ilmenites and titanomagnetites are mostly found in the groundmass. Chrome spinels present a scattered composition with 19.2–43.9 wt.% FeO, 14.8–47.2 wt.% Cr_2O_3, 0.9–6.8 wt.% TiO_2, 12.3–32.3 wt.% Al_2O_3 (Table S4 in supplementary material). Ilmenite and titanomagnetite are the most abundant oxides, with FeO and TiO_2 contents varying from 49.3 to 83 wt.% and 4.2–21.3 wt.%, respectively.

Perovskite microcrystals have been identified in sample MOZ01-DW05–03, with contents of 56 wt.% for TiO_2 and 36 wt.% for CaO, on average (Table S6 in supplementary material).

4.4.5. Biotite, phlogopite, and amphibole

Biotite is found in some samples as a primary phase. In MOZ01-DW05–13 Hall Bank sample, biotite antecrystals, with Mg# ranging from 38.4 to 42.4 (Table S5 in supplementary material), are surrounded by a reaction rim, and sometimes have an irregular shape. Different processes have been proposed to explain the development of

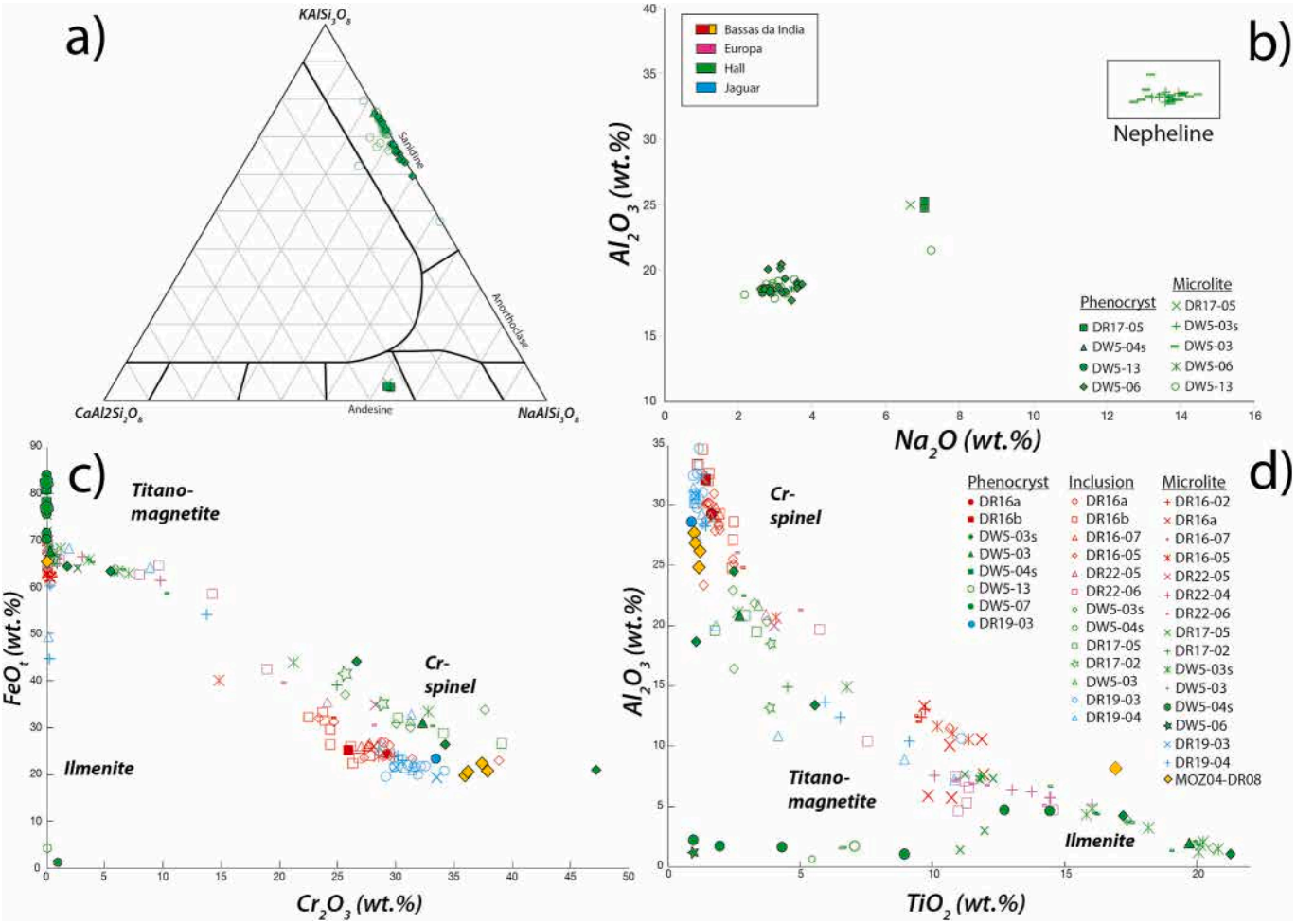

Fig. 8. Feldspar and Fe—Ti oxide compositions analyzed in dredged samples. a) Ternary diagram showing the compositions of alkali feldspar and plagioclase, b) Al_2O_3 vs Na_2O diagram showing the composition ranges for feldspar and nepheline, and c - d) FeO vs Cr_2O_3 and Al_2O_3 vs TiO_2 diagrams showing Fe—Ti oxide compositions.

destabilization rims for biotite. These include intrusion of a hot, more primitive magma (France, 2020) and reheating above the biotite liquidus (Grocke et al., 2015), or magma degassing upon rapid decompression during magma ascent (France, 2020). Crystals present a complex BaO zoning with compositional variations within several micron-wide zones (Fig. 6b). Biotite crystals are also to be found in small proportions in Hall Bank samples MOZ01-DW05–03, MOZ01-DW05–04 (Mg# = 50.1), MOZ01-DW05–06 (Mg# = 59.3–60.3), and in Bassas da India samples (MOZ04-DR08 and MOZ01-DR16a). Phlogopite crystals can be found in sample from Jaguar Bank (MOZ01-DR19–06 - Mg# = 71.5).

In Hall Bank samples (MOZ01-DW05–04, MOZ01-DW05–06, MOZ01-DW05–07, and MOZ01-DW05–09), calcic amphibole is mainly found as rare macrocrystals. These amphibole crystals vary slightly in composition (Mg# = 76.0–77.1, Table S5 in supplementary material) from one sample to another, and in some cases even within a given sample. In Bassas da India and Jaguar Bank samples, calcic amphibole crystals are observed as groundmass phase (Mg# = 26.2–36.5).

4.4.6. *Accessory phases*

The main accessory phases observed in our samples are titanite and apatite. Titanite has been found occasionally in Hall Bank samples and displays CaO and TiO_2 contents at 25.5–28.32 wt.% and 34.62–36.85 wt.%, respectively (Table S6 in supplementary material). In Hall Bank sample MOZ01-DW05–13, apatite is observed as microcrysts, while in Europa samples, apatite appears as inclusions in clinopyroxene crystals, and as rare crystals in the groundmass.

In all Hall Bank tephri-phonolite samples (MOZ01-DW05–04, MOZ01-DW05–06, MOZ01-DW05–07, MOZ01-DW05–08, MOZ01-DW05–09, and MOZ01-DW05–13), dolomite macrocrystals have been found in the lava. Their Ca/Mg ratio is mostly between 1.8 and 2.4 (Table S6 in supplementary material). In addition, in the samples MOZ01-DW05–03, MOZ01-DW05–04, and MOZ01-DW05–08, Ti-rich garnets (melanite, schorlomite) have been observed and analyzed. They are characterized by 27.8–31.4 % SiO_2, 9.36–14.4 % TiO_2, 31.1–31.9 % CaO, 18.6–20.84 % FeO.

4.5. *Alteration phases*

Studied samples are dredged rocks of Miocene age (Berthod et al., 2022a) that have spent several million years underwater. They were found to be highly altered, with high LOI values (Fig. 9a). This alteration takes various forms (Fig. 9). It consists of the transformation of the vitreous and microlitic groundmass into alteration paragenesis (clay minerals, carbonates, sulphates, phosphates, oxides, and hydroxides, etc. - Table S7 in supplementary material) and probably amorphous material, the replacement of primary minerals such as olivine or plagioclase feldspar by alteration minerals, and the crystallization of secondary phases in vesicles, cracks, and mineral relics (carbonates, zeolites, gypsum, etc.). Whenever possible, these phases were identified using a combination of SEM observations, microprobe analysis, and Raman spectrometry.

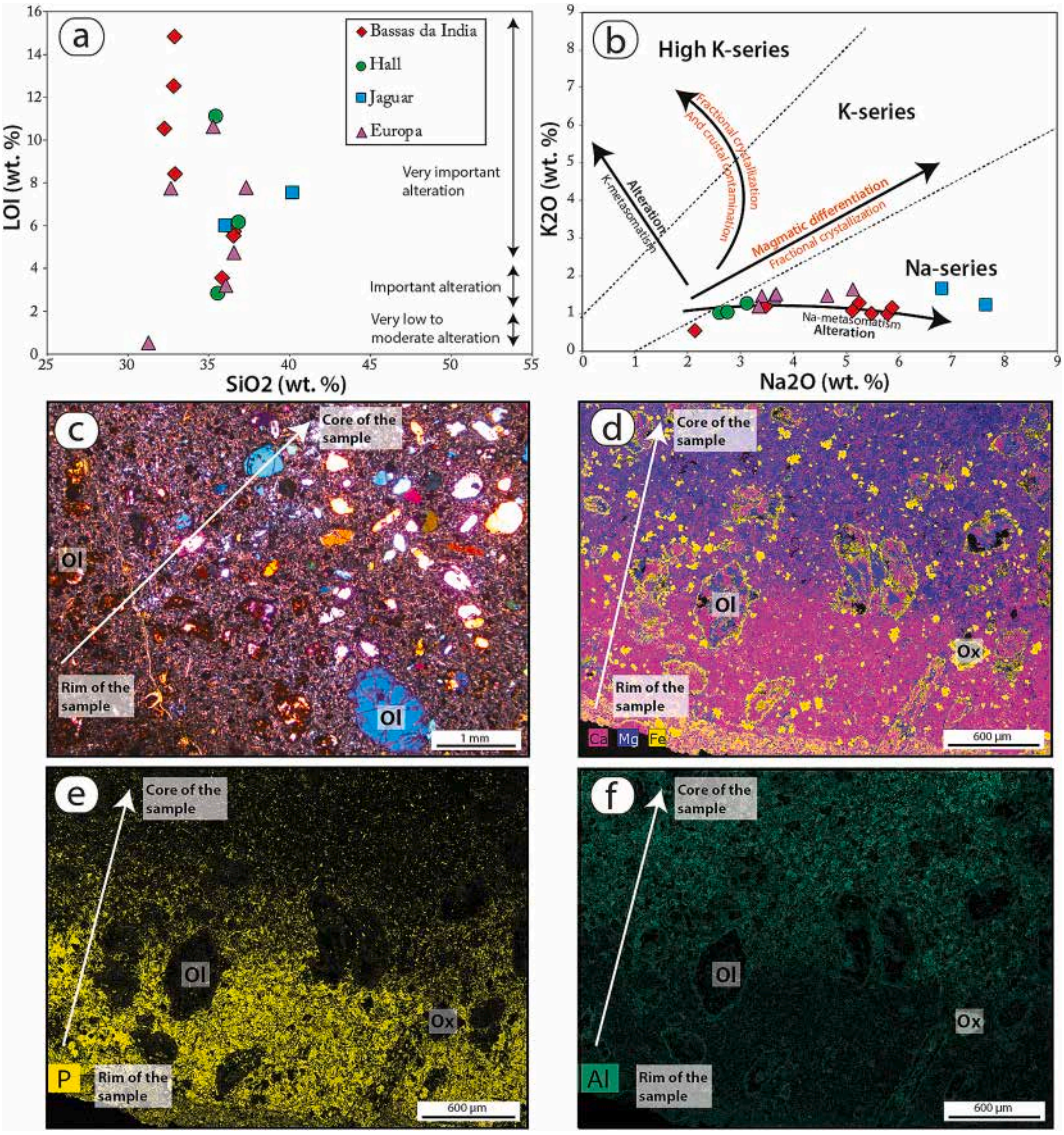

Fig. 9. Evidence and characteristics of the alteration observed in our dredged samples. a) SiO_2 vs LOI diagram highlighting the significant alteration of our samples. b) K_2O vs Na_2O diagram showing Na-metasomatism. c) Thin-section of the MOZ01-DW05–03 sample showing altered olivine in the rim of the sample. d-f) Ca, Mg, Fe, P, and Al elements maps in the MOZ01-DW05–03 sample.

Pyroxene and spinel crystals are largely preserved. The most common reaction consists of partial or even complete replacement of olivine crystals by iddingsite, clay minerals, or Mg-calcite (Figs. 4a, 9c). Low-Mg calcite is a phase commonly found in our samples, in association with olivine. Aragonite has also been identified in Bassas da India samples MOZ04-DR08. Calcite usually corresponds to late-stage products in interstices, fissures, and vesicles, but also appears as inclusion in some olivine crystals in Jaguar Bank samples (Fig. 3a). The composition of calcite in these inclusions (major elements) does not significantly differ from that of calcite found in vesicles, with CaO and MgO contents at 45.97–57.65 wt.% and 0–3.38 wt.%, respectively. In the same samples, vesicles may contain Na-rich feldspar crystals surrounded by Mg-calcite. Motukoreaite (e.g., Rodgers et al., 1977) has also been identified as inclusion in some olivine crystals, associated with euhedral clinopyroxene microcrystals (MOZ01-DR19–04), as was hydrotalcite in the matrix of the MOZ01-DW05–03 sample.

Secondary minerals such as oxides and hydroxides (hematite, goethite, Mn-oxides), phyllosilicates (chlorite, vermiculite, biotite, montmorillonite, saponite), have been identified by Raman spectrometry (see supplementary material) in several samples from Bassas da India (MOZ01-DR16, MOZ04-DR08), Hall Bank (MOZ01-DW05), and Europa (MOZ01-DR22). In the vesicles and fissures of the samples, in addition to calcite, various types of fibrous or isometric zeolites (phillipsite, chabazite, erionite, heulandite) were frequently found.

These mineral parageneses suggest low-temperature alteration, probably as a result of CO_2-rich fluids and seawater interaction, as evidenced by the more extensive alteration on the margins of samples in contact with seawater. The role of Na-metasomatism induced by rock-seawater interaction is supported by the whole-rock geochemistry with an enrichment in Na_2O content relative to K_2O which cannot be attributed to magmatic differentiation or fractional crystallization (Fig. 9b). The influence of this low-temperature alteration on the chemical composition of the whole rock has been assessed by comparing the chemical composition of the rim and core of the sample MOZ01-DW05–03 (Fig. 9d-f). The rim appears enriched in CaO, Al_2O_3, P_2O_5, and FeO, and depleted in SiO_2 and MgO.

4.6. Bulk-rock geochemistry

4.6.1. Major element compositions

Major and trace element whole-rock analyses for 15 samples are presented in Table S8 in supplementary material. Only mafic samples collected by dredging could be analyzed. Samples of the most differentiated lavas, only collected as pebbles at the top of Hall Bank, were too small for chemical analysis. As mentioned before, these samples are therefore characterized on the basis of their texture and mineralogical composition only.

All the analyzed samples have high LOI (loss on ignition) values, up to 14.8 wt.% (Table S8 in supplementary material). This certainly reflects the strong alteration of the rocks analyzed, but may also be partly due to a high volatile content (primarily CO_2). High LOI values are quite common worldwide for alkaline ultrabasic rocks (e.g., Lustrino et al., 2021).

For the geochemical approach, we selected fragments judged to be visually the most preserved, while trying to retain enough samples to obtain the most relevant information for the entire studied region. The state of preservation of our samples must be considered, and our results have therefore been interpreted only qualitatively, using trends and relying on bibliographical data. Only samples with a LOI value of less than 8 will be considered below.

All samples are alkaline, strongly undersaturated and belong to the "foidite" field according to the TAS nomenclature scheme (Le Maitre et al., 2005, Fig. S1 in supplementary material), with low SiO_2 concentrations (32.7–40.1 wt.% SiO_2) and rather high concentrations of alkalis for the silica content (1.6–4.9 wt.% $Na_2O + K_2O$). Their K_2O/Na_2O ratio (av. 0.63 ± 0.1) places most of these samples in the potassic series of Middlemost (1975), except for some samples from Bassas da India (MOZ01-DR16–02 and MOZ01-DR16–03) and Jaguar Bank (MOZ01-DR19–03) which are part of the sodic series ($K_2O/Na_2O < 0.5$). Because our samples are altered, we also use the Zr/TiO2*10^-4 - Nb/Y diagram (Lang et al., 2023), which confirms that these lavas are mainly located in the Alkali Basalt-Basanite-Foidite field (Fig. S2 in supplementary material).

Major element compositions on whole-rocks show a well-defined trend (Fig. 10a-b). Samples from Bassas da India and Jaguar Bank display the most basic compositions with MgO contents ranging from 14.2 to 17.7 wt.% and from 12.4 to 12.9 wt%, respectively (Fig. 10a-b). MgO content is lower in Hall Bank and Europa samples, and varies from 10.3 to 11.1 wt% and from 5.9 to 7.6 wt.%, respectively. K_2O content is inversely correlated to MgO content (Fig. 10a). Europa samples display the most differentiated compositions, with the highest K_2O contents, ranging from 1.2 to 1.6 wt.%. K_2O content in Bassas da India samples ranges from 0.55 to 1.16 wt%, while Hall and Jaguar Banks samples have K_2O contents between 1.02 and 1.68 wt.%. CaO/Al_2O_3 ratios are ranging from 0.7 to 1.1 wt.%, 1.0–1.7 wt.% and from 1.4 to 1.8 wt.% for Bassas da India, Jaguar and Hall Banks, and Europa samples, respectively (Fig. 10b). Fe_2O_3 contents of Bassas da India samples are clustered at 11.9–1.8 wt.%, while Hall and Jaguar Banks present more scattered Fe_2O_3 contents (9.5 to 14.5 wt.%). Fe_2O_3 content in Europa samples is characterized by high values, from 16.8 to 18.1 wt.%.

4.6.2. Trace element compositions

The chondrite-normalized rare earth element (REE) patterns obtained from the dredged samples are shown in Fig. 10c. All samples have steep chondrite-normalized REE patterns, showing a strong enrichment in light REE (LREE) compared to heavy REE (HREE), with no Eu anomaly. However, some minor distinctions can be mentioned. Europa samples are less fractionated in LREE in comparison to other samples, while MOZ01-DR19–03 Jaguar Bank sample is less enriched and shows a more concave REE pattern compared to those of Bassas da India and Hall Bank. LREE/HREE ratios are higher in Bassas da India and Hall Bank lavas ($(La/Yb)_N$ = 33.7 and 26.9–29.4, respectively) than those of Jaguar Bank and Europa ($(La/Yb)_N$ = 20.2–21.9 and 18.5–23.7, respectively). All samples display similar spider diagrams of incompatible trace elements normalized to Primitive Mantle concentrations with a depletion in Pb, Sr, K, and Ti, and a positive P anomaly (Fig. 10d).

Dredged samples are characterized by a well-defined trend of increasing Zr, with values ranging from 240 to 432 ppm with decreasing Mg# (Fig. 10e). Europa and Hall Bank samples are slightly more enriched in incompatible elements than Bassas da India and Jaguar Bank lavas. Indeed, Zr contents vary from 360 to 432 ppm in Europa and Hall Bank samples and from 240 to 334 ppm in Bassas da India and Jaguar Bank samples. In comparison, Ni concentrations, with values ranging from 99 to 302 ppm, show a weaker correlation with Mg# (Fig. 10f). Europa and Bassas da India samples display a quite low Ni content (99 to 162 ppm) and are not located on the Ni-Mg# trend. Similar observation has been made with Cr contents. Samples of Hall Bank are characterized by lower Ni content varying from 139 to 158 ppm.

4.6.3. Isotopes

Nd–Sr–Pb isotope data of dredged volcanic rocks are presented in Fig. 11 and in Table S8 in supplementary material. Our entire data set is characterized by a rather narrow isotopic range for Nd and Pb. Only $^{87}Sr/^{86}Sr$ ratios display a larger variation, ranging from 0.703796 to 0.708196 (Fig. 11a). These values were obtained on both leached and unleached samples, and the two most radiogenic isotope compositions (unleached samples) are very likely the result of seawater alteration (Verma, 1981).

With $^{143}Nd/^{144}Nd$ and $^{206}Pb/^{204}Pb$ ratios ranging from 0.512818 to 0.512878 and from 19.2381 to 19.9866, respectively, our samples have isotopic compositions similar to those of La Grille volcano in Comoros Archipelago (Fig. 11a-c, Class and Goldstein, 1997; Class et al., 1998; Class et al., 2005, 2009; Deniel, 1998; Pelleter et al., 2014; Späth et al., 1996), and the Cenozoic volcanism on Madagascar (Cucciniello et al., 2011; Cucciniello et al., 2017; Cucciniello et al., 2023; Melluso et al., 2007b; Melluso et al., 2016; Melluso et al., 2018). We also note that our samples differ from Cenozoic volcanism of the Rungwe volcanic province, in southern Tanzania (Castillo et al., 2014) and the Mozambique Ridge (Jacques et al., 2019; O'Connor et al., 2019), with higher $^{206}Pb/^{204}Pb$ and $^{208}Pb/^{204}Pb$ (39.1107–39.9207, Fig. 11b-d) ratios.

5. Discussion

5.1. Melting and mantle source

Recent studies suggest that the mantle sources of the Cenozoic alkaline volcanism of the northernmost part of Madagascar and Comoros archipelago are enriched in trace elements and volatiles, and have a genetic link to a HIMU-type mantle lithosphere (Chauvel et al., 2024; Cucciniello et al., 2023; Pelleter et al., 2014). The mantle source involved in the genesis of these volcanic provinces is considered to be chemically and mineralogically heterogeneous at small scale, with different degrees of metasomatism (Class and Goldstein, 1997; Cucciniello et al., 2023; Pelleter et al., 2014; Späth et al., 1996), and the presence of recycled hydrothermally altered oceanic crust in the mantle source (Chauvel et al., 2024). The dataset obtained from the Miocene dredged rocks provides an initial overview of the source of magmatism in the southern part of the Mozambique Channel, except for Sr isotopic data on leached samples, which might reflect the influence of seawater alteration and will not be discussed further in this paper. All the Bassas da India-Europa volcanic rocks show small Nd and Pb isotopic variations (Fig. 11), suggesting derivation from a common mantle source. In addition, the isotopic compositions of Pb and Nd are close to those known for Cenozoic volcanism in northern Madagascar and the Comoros archipelago. On the contrary, they significantly differ from those of the central and southwestern volcanic provinces of Madagascar with higher $^{143}Nd/^{144}Nd$, $^{206}Pb/^{204}Pb$, $^{207}Pb/^{204}Pb$, and $^{208}Pb/^{204}Pb$ (Fig. 11), whereas petrological observations, major whole-rock compositions, and age ranges are quite similar (Miocene, see Berthod et al., 2022a). Trace

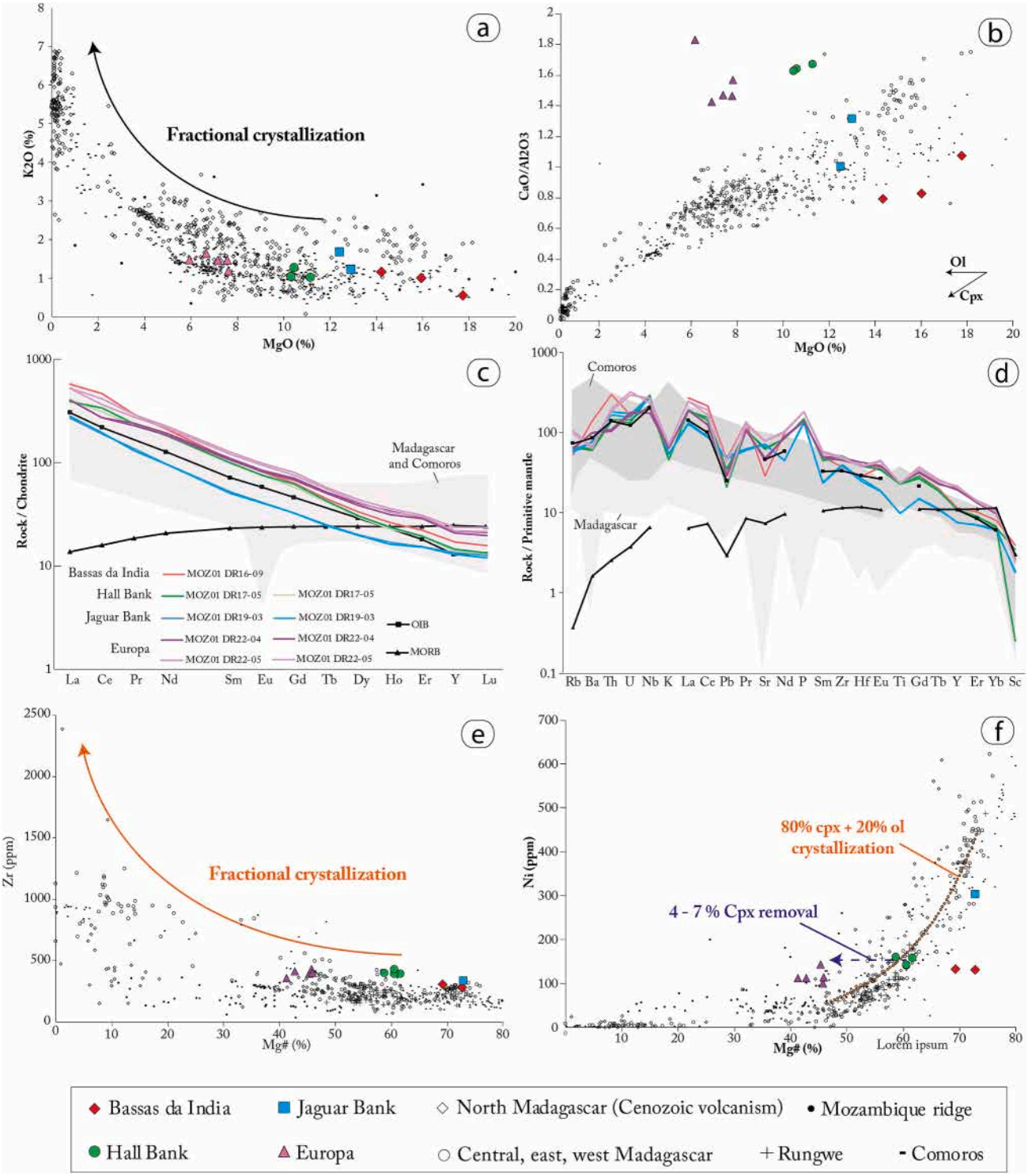

Fig. 10. Geochemistry of the dredged samples compared with lavas from Rungwe volcanic province (Marcelot et al., 1989; Furman, 1995), Mozambique ridge (O'Connor et al., 2019), Cenozoic volcanism on Madagascar (Cucciniello et al., 2011; Cucciniello et al., 2016; Cucciniello et al., 2017; Cucciniello et al., 2023; Melluso et al., 2000; Melluso et al., 2007a; Melluso et al., 2007b; Melluso et al., 2016; Melluso et al., 2018; Nougier et al., 1986), and Comoros Archipelago (Thompson and Flower, 1971; Strong, 1972; Nougier et al., 1986; Späth et al., 1996; Class and Goldstein, 1997; Class et al., 1998; Berthod et al., 2021a, 2021b, 2022b). a) K_2O vs MgO diagram showing fractional crystallization as a major process. b) MgO vs. CaO/Al_2O_3 diagram, and c) Chondrite-normalized REE patterns (Lyubetskaya and Korenaga, 2007) of selected samples. d) Primitive mantle-normalized patterns (Lyubetskaya and Korenaga, 2007) of our samples showing negative K, Pb, Ti, and positive P anomalies. e) Zr vs Mg# diagram displaying fractional crystallization effect. f) Back-crystallization models from Berthod et al. (2021a) implying 80 % clinopyroxene and 20 % olivine fractionation. This back calculation models start from a basanitic composition (Berthod et al., 2021a) by adding in small increments of equilibrium olivine and clinopyroxene compositions appropriate to match the composition of subaerial Comoros lavas, and consistent with the Ni concentration for a primary mantle melt (300–500 ppm, Späth et al., 1996).

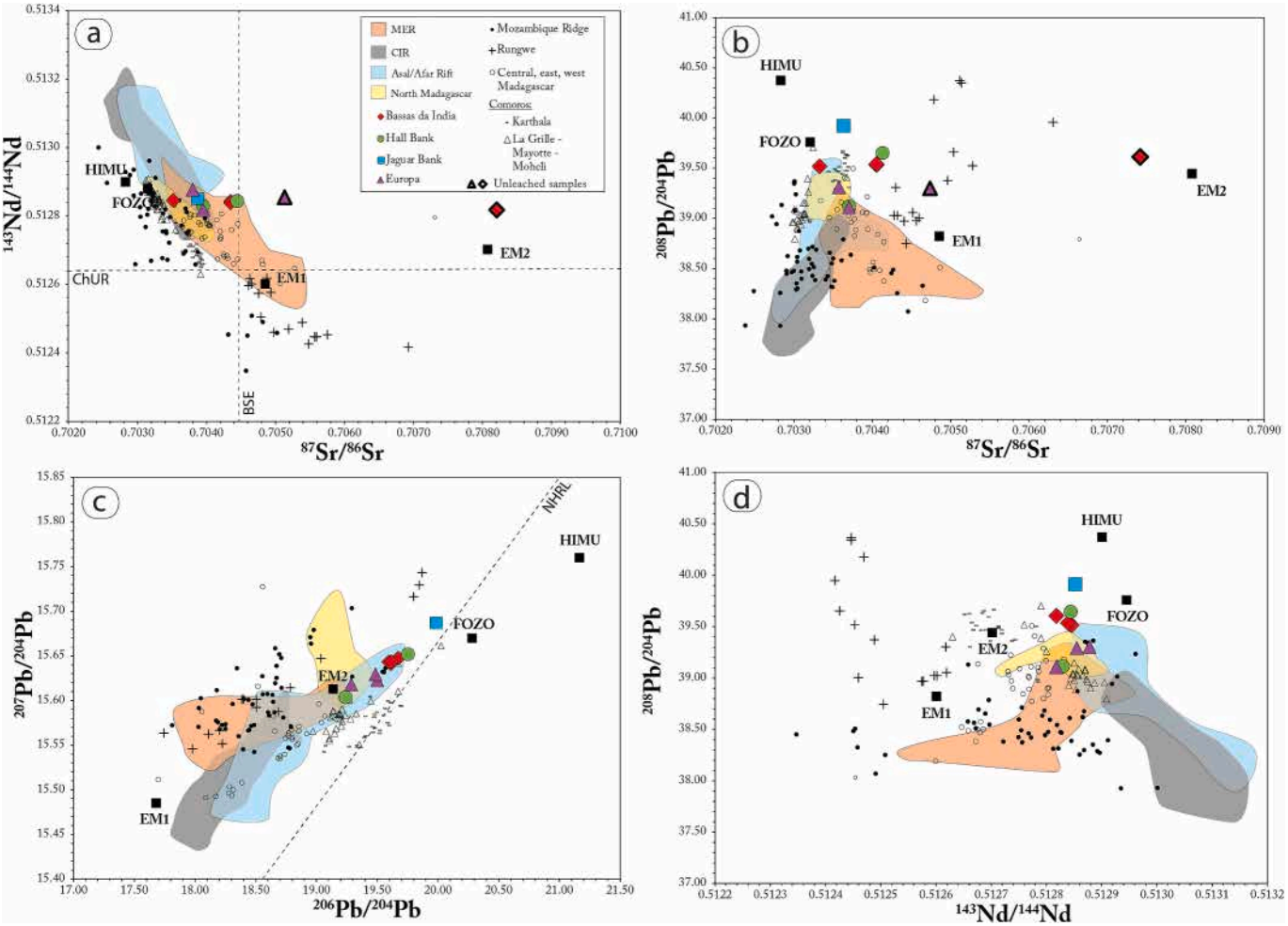

Fig. 11. Sr-Nd-Pb isotope variation diagrams for samples from Bassas da India/Europa volcanic province compared with Cenozoic volcanism in Madagascar (Cucciniello et al., 2011; Cucciniello et al., 2017; Melluso et al., 2007b; Melluso et al., 2016; Melluso et al., 2018), Comoros archipelago (Class and Goldstein, 1997; Class et al., 1998; Class et al., 2005, 2009; Deniel, 1998; Pelleter et al., 2014; Späth et al., 1996), Rungwe volcanic province (Castillo et al., 2014), the Mozambique Ridge (Jacques et al., 2019; O'Connor et al., 2019), and the Main Ethiopian Rift (MER) and the Central Indian Ridge (CIR). ChUR: Chondritic Uniform Reservoir; BSE: Bulk Silicate Earth; NHRL: Northern Hemisphere Reference Line.

element compositions (Fig. 10) also display few differences between our samples and those of the central and southwestern Cenozoic volcanic provinces of Madagascar.

Most of the studied samples have highly enriched chondrite-normalized REE patterns (Fig. 10c), with $(La/Yb)_N$ values between 18.6 and 33.7. In the Pearce (2008) Th/Yb-Nb/Th and TiO_2/Yb-Nb/Th diagrams (Fig. 12a, b), whole-rock compositions plot within the OIB field, suggesting that these magmas originate from a deep mantle source (high mean pressure and low partial melting rate). Both the primitive mantle-normalized multi-element variation and REE patterns also indicate that the Europa-Bassas da India lavas are geochemically close to OIB (Fig. 10c-d).

Chondrite-normalized REE patterns (Fig. 10c) combined with HREE ratios (Tb_N/Yb_N = 1.8–2.9) suggest that melts were formed through melting of an enriched mantle source within the garnet's stability field, at depths greater than 80 km. Using trace element ratios, coupled with a model of partial melting, Bassas da India-Europa lavas appear to have formed from magmas generated by less than 5 % partial melting of a mantle source within the spinel and garnet stability fields (Fig. 12c). Using batch modeling calculated for a moderately enriched source (Table 3 in Pouclet et al., 2016) with modal compositions of spinel-lherzolite (olivine 53 %, opx 27 %, cpx 17 %, spinel 3 %) and garnet-lherzolite (olivine 60 %, opx 20 %, cpx 10 %, garnet 10 %), we suggest that the source of Bassas da India and Europa magmas is spinel- and garnet-bearing lherzolite. Variations in trace elements ratios could be the result of small-scale chemical and mineralogical variations. Hall Bank Sm/Yb ratios, ranging from 6.3 to 6.5, are higher than those of Bassas da India and Europa magmas suggesting a source more enriched in garnet (Fig. 12c). In contrast, Jaguar Bank Sm/Yb ratio (MOZ01-DR19–03 = 3.6) is lower, supporting a source less enriched in garnet. This nature and garnet content differences might also be interpreted as a difference of partial melting depth. Thus, we can suggest that the melting source of the Hall Bank magma, more enriched in garnet, is probably deeper than those from Bassas da India, Europa, and then Jaguar Bank (Fig. 12c). Trace and rare-earth elements also indicate that lavas result from a low degree of partial melting (< 5 % - Fig. 12c) in agreement with their strongly silica-undersaturated and alkaline compositions. Nevertheless, using rare earth elements, we suggest that these degrees of partial melting vary through the archipelago with a lower degree of partial melting for Jaguar Bank magmas and highest degrees for Bassas da India and Europa (Fig. 12c).

5.2. *Evidence of metasomatism*

Metasomatism in the source has previously been highlighted throughout the volcanic provinces in the Mozambique Channel. In the northern half of Madagascar, Cenozoic volcanism of the Alaotra, Takarindoha–Vatomandry, and Votovorona volcanic fields are

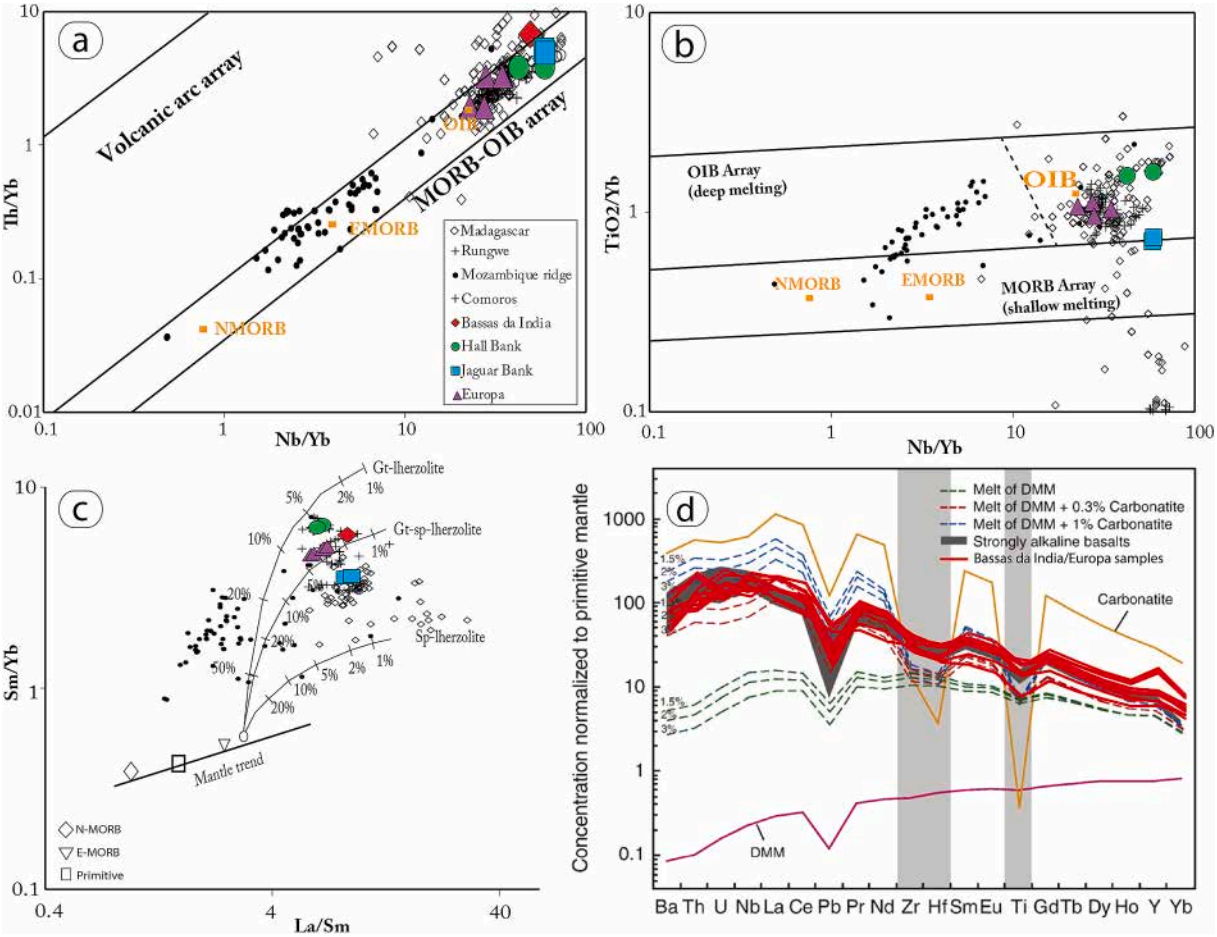

Fig. 12. Nature of source of Bassas da India-Europa volcanism and degree of partial melting. a) Th/Yb–Nb/Yb and b) TiO_2/Yb–Nb/Yb diagrams. c) La/Sm vs Sm/Yb diagram annotated with partial melting curves for garnet and spinel lherzolite mantle sources (Pouclet et al., 2016). d) Results of trace element modeling of the melting of carbonated mantle from Zeng et al. (2017) compared to our samples. The primitive mantle values are from Lyubetskaya and Korenaga (2007).

interpreted as low-volume, low-degree melts of a garnet peridotite, fertilized by dolomitic metasomatism (Melluso et al., 2011). In the northernmost Madagascar, the rocks of the Massif d'Ambre are inferred to be the product of small degrees of partial melting (3–5 %) of an enriched peridotitic source showing different degrees of metasomatism (Melluso et al., 2007; Melluso et al., 2016; Cucciniello et al., 2023). In the Comoros archipelago, geochemical studies suggest that lavas are mainly generated by partial melting of a DMM–HIMU CO_2-metasomatized mantle (Class et al., 1998; Class and Goldstein, 1997; Pelleter et al., 2014; Späth et al., 1996).

Beyond the effects potentially due to alteration, several indicators in the petrological and geochemical signature of Bassas da India-Europa volcanic province seem to support the presence of a mantle source fertilized by carbonatitic liquids:

(1) Our samples are characterized by low SiO_2 (32.2–40.1 wt.%), high CaO/Al_2O_3 (0.7–1.8 wt.%) and MgO (5.9–17.7 wt.%) contents (Fig. 10b). In addition, Bassas da India and Europa lavas are enriched in incompatible elements such as TiO_2 (2.2–3.7 wt%), Zr (178–432 ppm), Nb (18–141 ppm) and Ba (111–1134 ppm, Table S8 in supplementary material). According to Melluso et al. (2011), these geochemical signatures indicate that the source of the Bassas da India and Europa lavas is enriched in Ca and incompatible elements over Na and K, and may contain high-Ca, low-Si minerals, such as dolomite.

(2) Our samples are characterized by a strong K depletion (Fig. 10d) which may be interpreted as the consequence of the mantle source being relatively potassium poor (e.g., Melluso and Morra, 2000), or as the result of partial melting in the presence of residual amphibole (Class et al., 1998; Class and Goldstein, 1997; Späth et al., 1996), or both (Melluso et al., 2007a). The presence of amphibole in the source of Bassas da India and Europa lavas is supported by low Rb/Sr (0.012–0.138) and high Ba/Rb (6.145–92.63) ratios. This could be evidence of a metasomatized oceanic lithospheric mantle beneath the archipelago.

(3) Using trace-element modeling of mantle melting, Zeng et al. (2017) and Baudouin and Parat (2020) demonstrated that the characteristics of carbonatitic metasomatism, with negative K, Zr, Hf, and Ti anomalies (Figs. 10 and 12d), can be reproduced with a low degree of batch melting of carbonated peridotite (0.3 to 1 % of carbonatite). Such carbonatitic metasomatism is consistent with the primitive-mantle normalized diagram revealing that our samples have negative K, Zr, Hf, and Ti anomalies (Figs. 10 and 12d).

(4) Sanidine phenocrysts in the MOZ01-DW05–13 sample are characterized by BaO zoning (Fig. 6). In some compositional zones, barium content can reach 6 % (Fig. 6a). We note that Al_2O_3 content increases, and K_2O and SiO_2 contents decrease with decreasing BaO. The incorporation of barium in the sanidine solid solution is thus governed by BaAl - KSi substitution, so that an increase of the Ba content induces a higher Al/Si ratio in the feldspar (Gaeta, 1998). Barium might come from the destabilization of corroded biotite xenocrysts which is currently a Ba-storage mineral (Fig. 6). However, it is not uncommon for biotite antecrysts to also be characterized by barium-zoning (Fig. 6b). Therefore, the crystallization of biotite antecrysts and sanidine phenocrysts occurred in the same Ba-rich environment. Two assumptions can be made from these observations. (i) The concentration of Ba in the

melts results from metasomatism in the source region by a residual liquid or (ii) the magma sampled an evolved Ba-rich magma batch during its ascent. In a recent paper, Chauvel et al. (2024) postulated that the basanites of Fani Maoré volcano (Mayotte) formed by melting of an unusual mantle source, enriched in Ba and CO_2 by the presence of a recycled and hydrothermally-altered basaltic crust rich in baryte.

(5) Carbonatitic metasomatism is sustained by the presence of dolomite crystals in more evolved lavas on Hall bank (MOZ01-DW05–13 and MOZ01-DW05–04, Fig. 5c, d).

(6) Finally, MOZ01-DW05–13 and MOZ01-DW05–04 samples also contain Ti-rich garnets (schorlomite, Fig. 5c, d) which are typical of alkaline rocks, especially those with a high degree of silica undersaturation (e.g., Keep and Russell, 1992). This paragenesis is typical of a metasomatism linked to the percolation of a carbonatitic melt (Vozniak et al., 2023), which is itself interpreted as resulting from the demixing of a silica-undersaturated, highly alkaline, and volatile-rich magma having undergone significant fractionation, coupled with liquid immiscibility during fractional crystallization.

5.3. Magma storage conditions

Berthod et al. (2022a) suggest, on the basis of a morpho-structural interpretation, that large seamounts and atolls of the Bassas da India-Europa complex were fed from a multi-level magma storage system, consisting of permanently connected deep and shallow reservoirs located at the sediment-crust and crust-mantle boundaries, i.e., ~ 7 and ~ 15 km depth, respectively (Leinweber et al., 2013; Mueller and Jokat, 2017).

The very primitive nature of some of the ultrabasic and basic samples collected from the volcanic basement of Hall and Jaguar Banks, and Bassas da India and Europa Islands (Table 1 and Fig. 10) is revealed by (i) their high clinopyroxene content or the presence of perovskite, which is a common phase in many mantle-derived undersaturated rocks, (ii) the high magnesian composition of the olivine crystals at equilibrium (up to Fo88), and (iii) the relatively high MgO content of the lavas, despite possible loss due to alteration. In addition, samples were collected on top of the Hall Bank carbonate platform (dredge MOZ01-DW05, Fig. 2), with more evolved paragenesis, including alkali feldspar phenocrysts (Table 1 and Figs. 5b and 6). Such bimodal volcanism is observed in many volcanic settings, especially in oceanic contexts and continental hotspots. They can result from (1) differentiation within multiple magma storage, (2) differentiation by reactive melt flow in mush reservoirs (Jackson et al., 2018), or (3) magma mixing (Reubi and Blundy, 2009). Whatever the mechanism, this bimodality, often coupled with the presence of zoned crystals resulting from a complex magma history (Fig. 6), and with the coexistence of phenocrysts and antecrysts, is symptomatic of the existence of magma reservoirs.

Furthermore, some clinopyroxene phenocrysts, such as those observed in Europa lavas (MOZ01-DR22–06, Fig. 4e) show complex zoning, with Mg# varying from 72 to 81. Such patterns imply crystal growth under changing conditions of pressure, temperature, or melt composition, as expected in a mafic mush or in a multi-level magma storage environment. Zoned alkali feldspar and biotite macrocrystals have also been found in the differentiated lavas of Hall Bank (DW05–13, Figs. 5 and 6), showing the existence of a fluctuating composition of the melt in equilibrium with these crystals, compatible with the functioning of a dynamic reservoir, frequently recharged with evolved magma that sustains the volcanic activity. Finally, our study presents ultramafic to evolved parageneses (Figs. 3 and 5), suggesting magmatic processes such as fractional crystallization. From these observations, we may propose that the volcanic activity that enabled the building of the main volcanic edifices was fed by one or more large magma storage levels.

In contrast, no zoned crystal has been observed in Jaguar and Bassas da India lavas. In these samples (Fig. 3c, d), clinopyroxene are mainly microlites with Mg# ranging from 69.1 to 73.9 that might suggest a more direct magma ascent from the mantle.

In the absence of a non-altered glass phase, geobarometric studies have been realized only with the "clinopyroxene-only" geobarometer of Putirka (2008). We have also tested the equilibrium mineral/whole-rock composition using Roeder and Rf (1970) and Putirka (2008) diagrams (Fig. 13). Thus, despite some variations, probably due to crystal fractionation/accumulation, we show that clinopyroxene and olivine compositions are consistent with the host rock compositions.

Despite the high degree of alteration of the rocks, clinopyroxene is a perfectly preserved phase in our samples. So, we can estimate the magma storage depth using the clinopyroxene composition geothermobarometer (Putirka, 2008) for Hall Bank, Jaguar Bank, Bassas da India, and Europa samples. Geobarometry estimations are presented in Fig. 14. Calculated pressures for Hall Bank samples range from 4.3 to 9.6 kbar, corresponding to depths of 14 and 32 ± 7 km assuming a density of 3000 $kg.m^{-3}$ for an oceanic crust, with corresponding temperatures of 965 and 885 °C (Table S9 in supplementary material). Similar values have been obtained from Bassas da India clinopyroxene with two clusters at 2.6–5.4 and 6.2–9.1 kbar, for temperatures of 959–1037 °C and 875–965 °C, respectively. Clinopyroxene crystals of Europa lavas also give two clusters at 3.1–3.9 kbar and 5.6–6.3 kbar, associated with 969–1054 °C and 957–967 °C, respectively, which suggests the presence of two magma reservoirs located at about 10 and 20 km depth (Fig. 14). Clinopyroxene crystals in Jaguar Bank samples display more complex patterns. Phenocrysts provide a range of values from 26 (one analysis) to 14–18 km depth (4.3 to 7.9 kbar), while microphenocrysts and phenocryst borders give a depth of 7–11.5 km (2.2 to 3.4 kbar). The calculated pressures are therefore consistent with the petrological observations. The associated temperatures vary between 944 °C (1 analysis), 1069–1144 °C and 1047–1149 °C, respectively.

The Bassas da India-Europa complex comprises both central, or shield, volcanoes, and diverging elongated volcanic ridges with monogenetic cones, ranging in height from > 10 to 665 m (Berthod et al., 2022a). The monogenetic volcanic cones are mapped mainly along the ridges, but also off-ridge, on the flanks of the seamounts (Fig. 2). The presence of these large volcanic cones in the distal sector, off the rift zones, suggests that they were more probably fed by a direct, poorly degassed magma, directly from a deep reservoir, bypassing the shallower storage zones, similarly to the current eruption offshore Mayotte (Berthod et al., 2021a, 2021b, 2022b). Consequently, we interpret the few calculated pressures corresponding to depths greater than 20 km, obtained for Bassas da India and Hall-Jaguar Banks (Fig. 14), as indicative of potential deep reservoirs within the mantle. The other values, between 9 and 15 km below the surface, may correspond to magma storage zones that overlap well with the crust-mantle boundary identified from seismic refraction (Leinweber et al., 2013; Mueller and Jokat, 2017). The existence of shallower magma storage (< 5 km depth, as proposed by Berthod et al., 2022a), allowing magma to intrude laterally into the rift zones to feed fissure eruptions building small volcanic cones and lava flows, is not confirmed by our geobarometric study. This shallow magma storage level, if it exists, may not be recorded by the crystallization of clinopyroxene because the residence times were too short, or our error bars are too large (about 10 km, Putirka, 2008), or simply not have been sampled by the dredging.

5.4. Magmatic processes

Although we have few geochronological constraints, it is clear that the most evolved lavas of Lower Miocene age, for which it has been shown that they come from the inner core of the Hall Bank edifice, are older than the more primitive, basic and ultrabasic lavas, of Upper Miocene age, collected from the flanks of the edifices. To understand the long-term functioning of these volcanic edifices, it is critical to understand how the most evolved magmas can be obtained from compositions that are similar or close to the most basic terms. In such a context of intraplate magmatism, typical magmatic processes such as crystal fractionation/accumulation or magma mixing during reservoir recharge

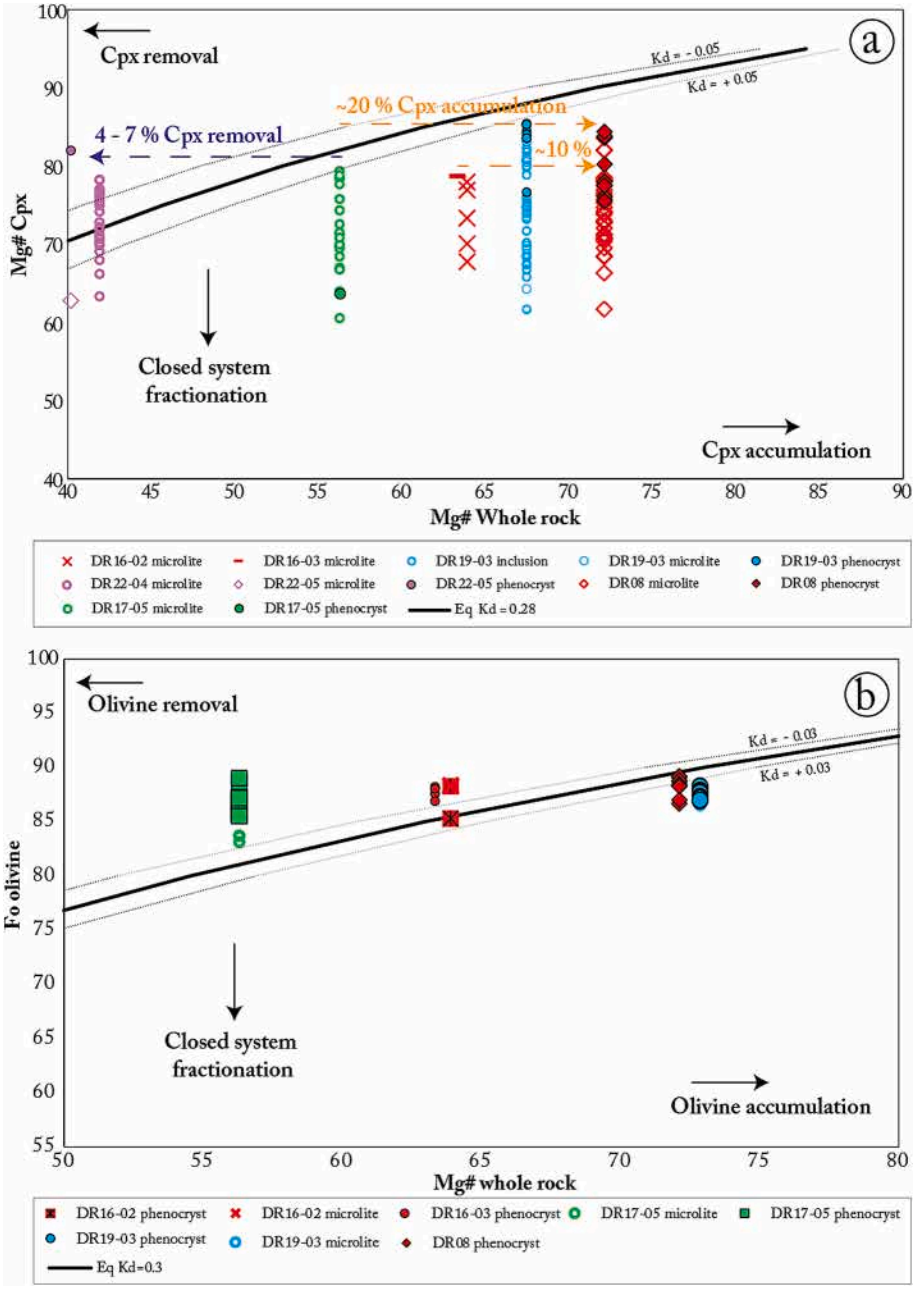

Fig. 13. Plot of a) clinopyroxene Mg number and b) olivine Fo content vs. whole-rock Mg number. Lines for $Kd^{Fe\text{-}Mg} = 0.30 \pm 0.03$ (Roeder and Rf, 1970) and $Kd^{Fe\text{-}Mg} = 0.28 \pm 0.05$ (Putirka, 2008) that reflect olivine-liquid and clinopyroxene-liquid equilibrium, respectively, are shown.

periods can explain the changes in temperature, pressure, or the availability of chemical elements in the different magma reservoirs that we have previously pinpointed using geobarometry.

Fractional crystallization.

The fractional crystallization process is supported by the behavior of major elements, which show, for example, an increase in K_2O content for a decrease in MgO content (Fig. 10a). Similarly, highly incompatible elements (such as Zr) increase with decreasing Mg#, whereas compatible elements decrease (Ni and Cr, Fig. 10f), which is consistent with fractional crystallization of olivine, spinel, and clinopyroxene, the main crystalline phases found in our samples from the basic series.

Bassas da India-Europa volcanic province lavas seem to follow a trend of decreasing Ni contents with decreasing Mg# (Fig. 10f). This trend, which suggests that lavas have experienced olivine and clinopyroxene fractionation, is superimposed to the Comoros lavas.

Since we have shown that the volcanic province displays similar geochemical signatures, ages and distributions, to the neighboring Miocene to Holocene volcanic provinces of the seaward extension of the EARS South-East branch, we can correlate magmatic processes of these provinces with those in the southern part of the Mozambique Channel. In the well described northern part of the Mozambique channel, several authors used trace element variations to model geochemical variations (Berthod et al., 2021a, 2021b, 2022b; Claude-Ivanaj et al., 1998; Späth et al., 1996) and fractional crystallization undergone by Comoros lavas. Since Jaguar and Hall Banks rock compositions are close to those of the Comoros (Figs. 10, 11, and 12), we suggest that they also have experienced 20 % olivine plus 80 % clinopyroxene fractionation and we applied the back-crystallization models from Berthod et al. (2021a). Nevertheless, Bassas da India and Europa samples cannot be reproduced only by the 20 % olivine plus 80 % clinopyroxene fractionation. Samples from Bassas da India display lower Ni content for higher Mg# (MOZ01-DR16–03, Fig. 10f). This difference in composition can be explained by

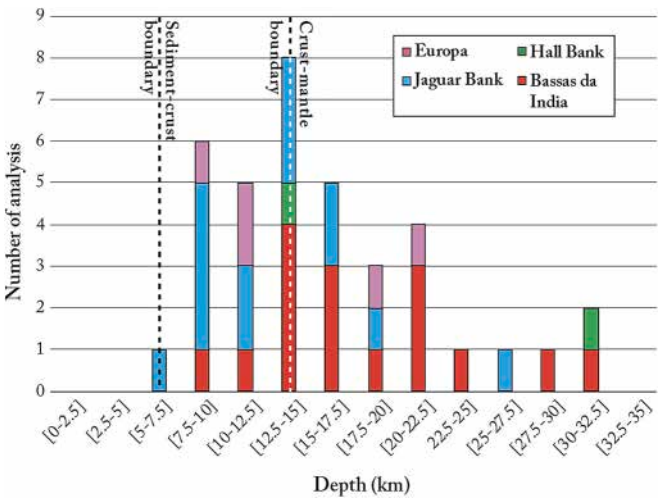

Fig. 14. Histogram to show depth (km) of clinopyroxene crystallization in Bassas da India, Hall Bank, Jaguar Bank, and Europa lavas calculated using Eq. 32a of Putirka (2008). Location of sediment-crust and crust-mantle boundaries is from Mueller et al. (2017).

(1) an accumulation of olivine and/or clinopyroxene crystals or (2) a more significant impact of alteration on the rock composition and its MgO content. In this case, the forsterite content would be more representative of the unaltered lavas than the composition of the whole-rock. MOZ01-DR16–03 sample is moderately porphyritic with Fo85–89 olivine and sometimes clinopyroxene as main macrocrystalline phases (Fig. 4). In addition, olivine crystals in MOZ01-DR16 dredges are in equilibrium with the whole-rock (Fig. 13b). From these geochemical data and our petrological observations, we suggest that the MOZ01-DR16–03 sample may be an altered primary liquid.

Europa samples display higher Ni content for lower Mg# (Fig. 10f). Two assumptions can be made: 1) the source is similar, but the fractional crystallization is different and involves a higher clinopyroxene content; 2) fractional crystallization is similar (80 % cpx + 20 % ol), but the nature of the source is different. While traces and rare-earth elements do not show mantle source variations (Figs. 10 and 12), we observe that clinopyroxenes in MOZ01-DR22 samples are not in equilibrium with the whole-rock and have higher Mg# than predicted by equilibrium conditions (Fig. 13a). According to a mass balance model, this disequilibrium can be explained by the removal of 4–7 % of clinopyroxene crystals, in consistency with the low proportion of crystals found in the samples (Fig. 4).

5.5. Reservoir recharge

Based on morpho-structural (Berthod et al., 2022a) and petrological considerations, we postulate the possibility of the existence of multiple magma reservoirs at different levels, as well as, for certain lavas, a rapid and direct ascent of magmas from their source. This raises the question of whether these reservoirs could have been filled by more primitive magma and therefore of magma mixing. The possibility of frequent recharges is consistent with the assumption that the feeding system of a volcano can be made up of an array of sills and dykes that grow incrementally by the amalgamation of new magmatic injections from depth (Sparks et al., 2019). Furthermore, magma chambers growing incrementally are characterized by reactive flow which might produce chemical differentiation that occurs within each intrusion before it solidifies, with more evolved melt accumulating at the top of the intrusion. This differentiation creates compositional contrasts, which might be the source of the observed bimodal volcanism (Jackson et al., 2018), as we can see for the Bassas da India-Europa system.

In most of our samples, the composition of the phenocrysts is, as expected, more primitive than microlites (Figs. 7 and 8). Since microlites crystallized after phenocrysts (Figs. 3, 4, and 5), this difference of composition could be explained by a simple fractional crystallization model. However, mineral-whole rock Fe—Mg equilibrium diagrams clearly suggest accumulation of clinopyroxene and olivine in some lavas (Fig. 13). Furthermore, in the MOZ01-DR16–07 sample, clinopyroxene phenocrysts have lower Mg# (ranging from 58.1 to 60.9) than clinopyroxene microlites (61.2–73.6, Fig. 7c, d, and Table S2). Consequently, the composition of microlites cannot result from the fractional crystallization of the magma that crystallized the phenocrysts. Rather, clinopyroxene microlites crystallized from a different, more primitive, later magma. This implies that magma storages are episodically replenished by new pulses of high-Mg magma.

5.6. The magmatism of the Bassas da India-Europa province integrated in the regional geodynamics

Bassas da India-Europa volcanic province displays a similar geochemical signature to the other neighboring Miocene to Holocene volcanic provinces of the seaward extension of the EARS South-East branch (Michon et al., 2022). In addition, the Miocene to Pleistocene province is spatially superimposed to an active seismicity already known in the region, the Quathlamba seismic axis, a 200 km-large fracture zone connected to the Davie Ridge transform system and interpreted to be the southward part of the East African Rift System (Berthod et al., 2022a; Michon et al., 2022). These similarities are also particularly true for the Comoros archipelago volcanism in the EARS Indian Ocean branch, which is characterized by the coexistence of active fault systems and Oligo-Miocene to Pleistocene alkaline volcanism (Spath et al., 1996; Class and Goldstein, 1997; Class et al., 1998; Deniel, 1998 ; Class et al., 2005, 2009; Pelleter et al., 2014; Berthod et al., 2021a, 2021b; Berthod et al., 2022b). From geochemical and tectonic observations, volcanism in the EARS South-East branch, which consists of small and scattered volcanic areas in the Mozambique Channel, has firstly been interpreted either as (1) the interaction of a mantle plume with oceanic lithosphere (Class et al., 1998; Class et al., 2005, 2009; Claude-Ivanaj et al., 1998; O'Connor et al., 2019) or as (2) the reactivation of lithospheric structures and regional extension possibly in relation with the onshore East African Rift System (Famin et al., 2020; Lemoine et al., 2020; Thinon et al., 2022).

Although close, the isotopic compositions of Bassas da India-Europa lavas do not fully overlap with the compositional fields of other known intraplate volcanic provinces in the Mozambique Channel (Fig. 11). Bassas da India-Europa lavas appear to have formed from magmas generated by less than 5 % partial melting of a mantle source within the spinel and garnet stability fields (Fig. 12c) which is not consistent with a strong influence of a mantle plume. Therefore, our study tends to support the hypothesis that the volcanism was likely associated with lithospheric deformation. One argument (Berthod et al., 2022a) is that the magma ascent is strongly controlled by large pre-existing crustal structures associated with the opening of the Mozambique Channel and the movement of the Davie ridge, formed as a consequence of the breakup of Gondwana, and of the ongoing southward propagation of the East African Rift System (Deville et al., 2018). This is also consistent with the Miocene to Holocene volcanic activity located in the Rungwe province (Marcelot et al., 1989; Furman, 1995), in the northern part of Madagascar (Cucciniello et al., 2023, 2011; Melluso et al., 2011; Melluso et al., 2007a) and in Comoros archipelago (Thinon et al., 2022), which have mainly been attributed to regional extension associated with the East African Rift System.

However, He-Sr-Nd–Pb-Os isotope ratios for the Comoros Archipelago (Class et al., 1998, 2005; Class and Goldstein, 1997; Pelleter et al., 2014; Späth et al., 1996) and Sr-Nd-Pb-Hf isotope ratios for the Mozambique Ridge (Jacques et al., 2019; O'Connor et al., 2019) support the geochemical influence of a mantle plume reported throughout the Mozambique Channel. Furthermore, tomography approaches (e.g.,

Tsekhmistrenko et al., 2021) suggests a slow velocity anomaly at 200 km depth with two directions of expansion: (1) To the east in the northern part of Madagascar and Mozambique Channel, and (2) to the southeast beneath South Africa.

A third hypothesis, which reconciles the two first ones, is proposed by Michon et al. (2022). They suggest a model involving an intricate relationship between the mantle and plate dynamic on which they interpret the EARS as the result of the combined effects of (1) extensive stresses acting on the African lithosphere in the long-lived context of the Gondwana breakup and (2) an overall complex dynamics of mantle upwelling. In such a context, we can suggest that the volcanism throughout the Mozambique Channel, and consequently that of the province of Bassas da India and Europa, would result from a thermal erosion of a heterogeneous and metasomatized mantle due to a mantle plume coupled to a lithospheric deformation. Similar geochemical signature, ages, and distribution of the EARS South-East and Indian Ocean branches involve a large-scale process and would be in line with this hybrid hypothesis.

6. Conclusion

Dredging realized during the PAMELA campaigns allowed us to characterize, for the first time, the volcanism in the southern part of the Mozambique Channel. Thus, despite a strong alteration, much information has been obtained, and our petrological and geochemical studies bring new constraints on the nature, the origin, and source of the volcanism. Moreover, it allows us to determine the petrogenetic processes and magmatic systems that fed this volcanic activity.

The Bassas da India-Europa volcanic province is characterized by a bimodal chemical distribution of erupted magmas, with nephelinite/basanite and intermediate lavas. Petrographic and geochemical investigations suggest that these lavas result from a low degree of partial melting near the garnet–spinel transition zone, between 80 and 100 km depth, of a garnet lherzolite, fertilized by dolomitic metasomatism.

The ascent of the magma passes through several long-life large and dynamic magma storage levels located in the mantle and at the crust/mantle and crust/sediment boundary zones at depths greater than 20 km, 15 km, and 5 km, respectively. In the crust, the magma ascent is strongly controlled by large preexisting N45–80° and N160–180° crustal faults. Our petrological study indicates that in this multiple magmatic system, the magmatic reservoirs are the site of repeated events of replenishment and fractional crystallization dominated by clinopyroxene and olivine.

Declaration of competing interest

The authors declare that they have no known competing financial interests or personal relationships that could have appeared to influence the work reported in this paper.

We confirm that we have no conflicts of interest related to this research, this work is original to its form and has not been published elsewhere, nor is under consideration for publication elsewhere.

Acknowledgements

We are grateful to Captain, Officers, and crew members of the PAMELA-MOZ01 (https://doi.org/10.17600/14001000) and PAMELA-MOZ04 (https://doi.org/10.17600/15000700) cruises onboard the R/V L'Atalante and R/V Pourquoi Pas? for their technical support in recovering high-quality dataset. The authors warmly thank Arnaud Gaillot and Delphine Pierre for bathymetry grids processing. The oceanographic expeditions PAMELA-MOZ01 and PAMELA-MOZ04 were co-funded by TOTAL and IFREMER as part of the PAMELA (Passive Margin Exploration Laboratory) scientific project, in collaboration with Université de Bretagne Occidentale, Université Rennes 1, Université Pierre and Marie Curie, CNRS et IFPEN.C. Berthod was supported by a PAMELA postdoctoral fellowship. We are also very grateful for the constructive reviews provided by Jörg Geldmacher and Peter Schaaf. This is contribution n°708 of the ClerVolc program of the International Research Center for Disaster Sciences and Sustainable Development of the University of Clermont Auvergne.

Appendix A. Supplementary data

Supplementary data to this article can be found online at https://doi.org/10.1016/j.lithos.2025.108155.

References

Baudouin, C., Parat, F., 2020. Phlogopite-olivine nephelinites erupted during early stage rifting, North Tanzanian Divergence. Front. Earth Sci. 8, 277. https://doi.org/10.3389/feart.2020.00277.

Berthod, C., Médard, E., Bachèlery, P., Gurioli, L., Di Muro, A., Peltier, A., Komorowski, J.-C., Benbakkar, M., Devidal, J.-L., Langlade, J., Besson, P., Boudon, G., Rose-Koga, E., Deplus, C., Le Friant, A., Bickert, M., Nowak, S., Thinon, I., Burckel, P., Hidalgo, S., Kaliwoda, M., Jorry, S.J., Fouquet, Y., Feuillet, N., 2021a. The 2018-ongoing Mayotte submarine eruption: Magma migration imaged by petrological monitoring. Earth Planet. Sci. Lett. 571, 117085. https://doi.org/10.1016/j.epsl.2021.117085.

Berthod, C., Médard, E., Di Muro, A., Hassen Ali, T., Gurioli, L., Chauvel, C., Komorowski, J.-C., Bachèlery, P., Peltier, A., Benbakkar, M., Devidal, J.-L., Besson, P., Le Friant, A., Deplus, C., Nowak, S., Thinon, I., Burckel, P., Hidalgo, S., Feuillet, N., Jorry, S., Fouquet, Y., 2021b. Mantle xenolith-bearing phonolites and basanites feed the active volcanic ridge of Mayotte (Comoros archipelago, SW Indian Ocean). Contrib. Mineral. Petrol. 176, 75. https://doi.org/10.1007/s00410-021-01833-1.

Berthod, C., Bachèlery, P., Jorry, S.J., Pitel-Roudaut, M., Ruffet, G., Revillon, S., Courgeon, S., Doucelance, R., 2022a. First characterization of the volcanism in the southern Mozambique Channel: Geomorphological and structural analyses. Mar. Geol. 445, 106755. https://doi.org/10.1016/j.margeo.2022.106755.

Berthod, C., Komorowski, J.-C., Gurioli, L., Médard, E., Bachèlery, P., Besson, P., Verdurme, P., Chevrel, O., Di Muro, A., Peltier, A., Devidal, J.-L., Nowak, S., Thinon, I., Burckel, P., Hidalgo, S., Deplus, C., Loubrieu, B., Pierre, D., Bermell, S., Pitel-Roudaut, M., Réaud, Y., Fouchard, S., Bickert, M., Le Friant, A., Paquet, F., Feuillet, N., Jorry, S.L., Fouquet, Y., Rinnert, E., Cathalot, C., Lebas, E., 2022b. Temporal magmatic evolution of the Fani Maoré submarine eruption 50 km east of Mayotte revealed by in situ sampling and petrological monitoring. Comptes Rendus Géosci. 354, 1–29. https://doi.org/10.5802/crgeos.155.

Castillo, P.R., Hilton, D.R., Halldórsson, S.A., 2014. Trace element and Sr-Nd-Pb isotope geochemistry of Rungwe Volcanic Province, Tanzania: implications for a superplume source for East Africa Rift magmatism. Front. Earth Sci. 2, 21. https://doi.org/10.3389/feart.2014.00021.

Chauvel, C., Inglis, E.C., Gutierrez, P., Luu, T.H., Burckel, P., Besson, P., 2024. Fani Maoré, a new "young HIMU" volcano with extreme geochemistry. Earth Planet. Sci. Lett. 626, 118529.

Class, C., Goldstein, S.L., 1997. Plume-lithosphere interactions in the ocean basins: constraints from the source mineralogy. Earth Planet. Sci. Lett. 150, 245–260.

Class, C., Goldstein, S.L., Altherr, R., Bachèlery, P., 1998. The process of plume–lithosphere interactions in the ocean basins—the case of Grande Comore. J. Petrol. 39, 881–903. https://doi.org/10.1093/petroj/39.5.881.

Class, C., Goldstein, S.L., Stute, M., Kurz, M., Schlosser, P., 2005. Grande Comore island: a well-constrained low $^{3}He/^{4}He$ mantle plume. Earth Planet. Sci. Lett. 233, 391–409. https://doi.org/10.1016/j.epsl.2005.02.029.

Class, C., Goldstein, S.L., Shirey, S.B., 2009. Osmium isotopes in Grande Comore lavas: a new extreme among a spectrum of EM-type mantle endmembers. Earth and Planetary tary Science Letters 284, 219–227. https://doi.org/10.1016/j.epsl.2009.04.031.

Claude-Ivanaj, C., Bourdon, B., Allègre, C.J., 1998. Ra–Th–Sr isotope systematics in Grande Comore Island: a case study of plume–lithosphere interaction. Earth and Planetary tary Science Letters 164, 99–117. https://doi.org/10.1016/S0012-821X(98)00195-2.

Counts, J.W., Jorry, S.J., Leroux, E., Miramontes, E., Jouet, G., 2018. Sedimentation adjacent to atolls and volcano-cored carbonate platforms in the Mozambique Channel (SW Indian Ocean). Mar. Geol. 404, 41–59. https://doi.org/10.1016/j.margeo.2018.07.003.

Courgeon, S., Jorry, S.J., Camoin, G.F., et al., 2016. Growth and demise of Cenozoic isolated carbonate platforms: New insights from the Mozambique Channel seamounts (SW Indian Ocean). Mar. Geol. 380, 90–105.

Courgeon, S., Jorry, S.J., Jouet, G., Camoin, G., BouDagher-Fadel, M.K., Bachèlery, P., Guérin, C., 2017. Impact of tectonic and volcanism on the Neogene evolution of isolated carbonate platforms (SW Indian Ocean). Sediment. Geol. 355, 114–131.

Cucciniello, C., Melluso, L., Morra, V., Storey, M., Rocco, I., Franciosi, L., Grifa, C., Petrone, C.M., Vincent, M., 2011. New 39Ar–40Ar ages and petrogenesis of the Massif d'Ambre volcano, northern Madagascar. In: Beccaluva, L., Bianchini, G., Wilson, M. (Eds.), Volcanism and Evolution of the African Lithosphere, 478. Geol. Soc. Am. Spec. Papers, pp. 257–282. https://doi.org/10.1130/2011.2478(14).

Cucciniello, C., Tucker, R.D., Jourdan, F., Melluso, L., Morra, V., 2016. The age and petrogenesis of alkaline magmatism in the Ampasindava Peninsula and Nosy be

archipelago, northern Madagascar. Mineral. Petrol. 110 (2), 309–331. https://doi.org/10.1007/s00710-015-0387-1.
Cucciniello, C., Melluso, L., le Roex, A.P., Jourdan, F., Morra, V., de Gennaro, R., Grifa, C., 2017. From olivine nephelinite, basanite and basalt to peralkaline trachyphonolite and comendite in the Ankaratra volcanic complex, Madagascar: 40Ar/39Ar ages, phase compositions and bulk-rock geochemical and isotopic evolution. Lithos 274, 363–382. https://doi.org/10.1016/j.lithos.2016.12.026.
Cucciniello, C., Grifa, C., de'Gennaro, R., et al., 2023. Alkaline rocks of the Bobaomby volcanic field point to a petrogenetic link between Comoros and northern Madagascar lithosphere. Int J Earth Sci (Geol Rundsch) 112, 707–723. https://doi.org/10.1007/s00531-022-02251-9.
Deniel, C., 1998. Geochemical and isotopic (Sr, Nd, Pb) evidence for plume–lithosphere interactions in the genesis of Grande Comore magmas (Indian Ocean). Chem. Geol. 144, 281–303. https://doi.org/10.1016/S0009-2541(97)00139-3.
Deville, E., Marsset, T., Courgeon, S., et al., 2018. Active fault system across the oceanic lithosphere of the Mozambique Channel: Implications for the Nubia–Somalia southern plate boundary. Earth Planet. Sci. Lett. 502, 210–220. https://doi.org/10.1016/j.epsl.2018.08.052.
Famin, V., Michon, L., Bourhane, A., 2020. The Comoros archipelago: a right-lateral transform boundary between the Somalia and Lwandle plates. Tectonophysics 789, 228539. https://doi.org/10.1016/j.tecto.2020.228539.
France, L., 2020. Can destabilization rims of hydrous minerals be used to constrain magma ascent kinetics at lava dome volcanoes? Bull. Volcanol. 82 (10), 66.
Furman, T., 1995. Melting of metasomatized subcontinental lithosphere: undersaturated mafic lavas from Rungwe, Tanzania. Contrib. Mineral. Petrol. 122 (1), 97–115. https://doi.org/10.1007/s004100050115.
Gaeta, M., 1998. Petrogenetic implications of Ba-sanidine in the Lionato Tuff (Colli Albani volcanic district, Central Italy). Mineral. Mag. 62, 697–701.
Gilfillan, S.M.V., Györe, D., Flude, S., et al., 2019. Noble gases confirm plume-related mantle degassing beneath Southern Africa. Nat. Commun. 10, 1–7.
Grocke, S.B., Andrews, B.J., Manga, M., Quinn, E.T., 2015. Magma Mixing Chronometry: Quantitative 3D Tomographic Analysis of Biotite Breakdown in Heating Experiments. AGU Fall Meeting Abstracts, In, pp. V11F–08.
Hartnady, C.J.H., 1985. Uplift, faulting, seismicity, thermal spring and possible incipient volcanic activity in the Lesotho-Natal Region, SE Africa: the Quathlamba Hotspot Hypothesis. Tectonics 4, 371–377.
Jackson, M.D., Blundy, J., Sparks, R.S.J., 2018. Chemical differentiation, cold storage and remobilization of magma in the Earth's crust. Nature 564, 405–409.
Jacques, G., Hauff, F., Hoernle, K., Werner, R., Uenzelmann-Neben, G., Garbe-Schönberg, D., Fischer, M., 2019. Nature and origin of the Mozambique Ridge, SW Indian Ocean. Chem. Geol. 507, 9–22.
Jorry, S., 2014. PTOLEMEE cruise. RV L'Atalante. https://doi.org/10.17600/14000900.
Jouet, G., Deville, E., 2015. PAMELA-MOZ04 cruise. Pourquoi pas ? https://doi.org/10.17600/15000700.
Keep, M., Russell, J.K., 1992. Mesozoic alkaline rocks of the Averill plutonic complex. Can. J. Earth Sci. 29 (11), 2508–2520. https://doi.org/10.1139/e92-197.
Kusky, T.M., Toraman, E., Raharimahefa, T., Rasoazanamparany, C., 2010. Active tectonics of the Alaotra–Ankay Graben System, Madagascar: possible extension of Somalian–African diffusive plate boundary? Gondwana Res. 18, 274–294.
Lang, M., Zhang, Z., Chen, Z., Cheng, Z., Santosh, M., Kusky, T.M., 2023. Classification and nomenclature of volcanic rocks using immobile elements: a novel approach based on big data analysis. Lithos 454, 107274.
Le Maitre, R.W., Streckeisen, A., Zanettin, B., et al., 2005. Igneous rocks: a classification and glossary of terms. Igneous Rocks a Classif Gloss terms. In: Ed by RW Le Maitre a Streckeisen B Zanettin MJ Le Bas B Bonin P Bateman, pp 252 ISBN 0521619483. UK Cambridge Univ Press, Cambridge. January 2005 252.
Leinweber, V.T., Klingelhoefer, F., Neben, S., et al., 2013. The crustal structure of the Central Mozambique continental margin—Wide-angle seismic, gravity and magnetic study in the Mozambique Channel, Eastern Africa. Tectonophysics 599, 170–196. https://doi.org/10.1016/j.tecto.2013.04.015.
Lemoine, A., Briole, P., Bertil, D., Roullé, A., Foumel, M., Thinon, I., Raucoules, D., de Michele, M., Valty, P., 2020. The 2018-2019 seismo-volcanic crisis east of Mayotte, Comoros islands: seismicity and ground deformation markers of an exceptional submarine eruption. Geophys. J. Int. 223 (1), 22–44. https://doi.org/10.31223/osf.io/d46xj.fr.
Lustrino, M., Salari, G., Rahimzadeh, B., Fedele, L., Masoudi, F., Agostini, S., 2021. Quaternary melanephelinites and melilitites from Nowbaran (NW Urumieh-Dokhtar Magmatic Arc, Iran): origin of ultrabasic-ultracalcic melts in a post-collisional setting. J. Petrol. 62 (9). https://doi.org/10.1093/petrology/egab058 egab 058.
Lyubetskaya, T., Korenaga, J., 2007. Chemical composition of Earth's primitive mantle and its variance: 1. Method and results. J. Geophys. Res. Solid Earth 112 (B3). https://doi.org/10.1029/2005JB004223.
Marcelot, G., Dupuy, C., Dostal, J., Rancon, J.P., Pouclet, A., 1989. Geochemistry of mafic volcanic rocks from the Lake Kivu (Zaire and Rwanda) section of the western branch of the African Rift. J. Volcanol. Geotherm. Res. 39 (1), 73–88. https://doi.org/10.1016/0377-0273(89)90022-X.
Melluso, L., Morra, V., 2000. Petrogenesis of late Cenozoic mafic alkaline rocks of the Nosy be archipelago (northern Madagascar): relationships with the Comorean magmatism. J. Volcanol. Geotherm. Res. 96 (1–2), 129–142. https://doi.org/10.1016/S0377-0273(99)00139-0.
Melluso, L., Morra, V., Riziky, H., et al., 2007a. Petrogenesis of a basanite–tephrite–phonolite volcanic suite in the Bobaomby (Cap d'Ambre) peninsula, northern Madagascar. J. Afr. Earth Sci. 49, 29–42.
Melluso, L., Morra, V., Brotzu, P., Franciosi, L., Grifa, C., Lustrino, M., Morbidelli, P., Riziky, H., Vincent, M., 2007b. The Cenozoic alkaline magmatism in Central-Northern Madagascar: a brief overview. Per Mineral 76, 169–180.
Melluso, L., le Roex, A.P., Morra, V., 2011. Petrogenesis and Nd-, Pb-, Sr-isotope geochemistry of the Cenozoic olivine melilitites and olivine nephelinites ("ankaratrites") in Madagascar. Lithos 127 (3–4), 505–521. https://doi.org/10.1016/j.lithos.2011.08.003.
Melluso, L., Cucciniello, C., Le Roex, A.P., Morra, V., 2016. The geochemistry of primitive volcanic rocks of the Ankaratra volcanic complex, and source enrichment processes in the genesis of the Cenozoic magmatism in Madagascar. Geochim. Cosmochim. Acta 185, 435–452. https://doi.org/10.1016/j.gca.2016.04.005.
Melluso, L., Tucker, R.D., Cucciniello, C., le Roex, A.P., Morra, V., Zanetti, A., Rakotoson, R.L., 2018. The magmatic evolution and genesis of the Quaternary basanite-trachyphonolite suite of Itasy (Madagascar) as inferred by geochemistry, Sr-Nd-Pb isotopes and trace element distribution in coexisting phases. Lithos 310, 50–64. https://doi.org/10.1016/j.lithos.2018.04.003.
Michon, L., Famin, V., Quidelleur, X., 2022. Evolution of the East African Rift System from trap-scale to plate-scale rifting. Earth Sci. Rev. 231, 104089. https://doi.org/10.1016/j.earscirev.2022.104089.
Middlemost, E.A., 1975. The basalt clan. Earth Sci. Rev. 11 (4), 337–364.
Mueller, C.O., Jokat, W., 2017. Geophysical evidence for the crustal variation and distribution of magmatism along the central coast of Mozambique. Tectonophysics 712, 684–703. https://doi.org/10.1016/j.tecto.2017.06.007.
Mueller, C.O., Jokat, W., 2019. The initial Gondwana break-up: a synthesis based on new potential field data of the Africa-Antarctica Corridor. Tectonophysics 750, 301–328. https://doi.org/10.1016/j.tecto.2018.11.008.
Nougier, J., Cantagrel, J.M., Karche, J.P., 1986. The Comores archipelago in the western Indian Ocean: volcanology, geochronology and geodynamic setting. J. Afr. Earth Sci. 5, 135–144. https://doi.org/10.1016/0899-5362(86)90003-5.
O'Connor, J.M., Jokat, W., Regelous, M., et al., 2019. Superplume mantle tracked isotopically the length of Africa from the Indian Ocean to the Red Sea. Nat. Commun. 10, 1–13. https://doi.org/10.1038/s41467-019-13181-7.
Olu, K., 2014. PAMELA-MOZ01 cruise. RV L'Atalante. https://doi.org/10.17600/14001000.
Pelleter, A.-A., Caroff, M., Cordier, C., et al., 2014. Melilite-bearing lavas in Mayotte (France): an insight into the mantle source below the Comores. Lithos 208, 281–297. https://doi.org/10.1016/j.lithos.2014.09.012.
Pouclet, A., Bellon, H., Bram, K., 2016. The Cenozoic volcanism in the Kivu rift: Assessment of the tectonic setting, geochemistry, and geochronology of the volcanic activity in the South-Kivu and Virunga regions. J. Afr. Earth Sci. 121, 219–246. https://doi.org/10.1016/j.jafrearsci.2016.05.026.
Putirka, K.D., 2008. Thermometers and Barometers for Volcanic Systems. Rev. Mineral. Geochem. 69, 61–120. https://doi.org/10.2138/rmg.2008.69.3.
Raillard, S., 1990. Les Marges de l'Afrique de l'Est et les Zones de Fracture Associées: Chaine Davie et Ride du Mozambique (PhD Thesis).. Université Pierre et Marie Curie, Paris VI.
Reubi, O., Blundy, J., 2009. A dearth of intermediate melts at subduction zone volcanoes and the petrogenesis of arc andesites. Nature 461, 1269–1273. https://doi.org/10.1038/nature08510.
Roche, V., Ringenbach, J.C., 2022. The Davie Fracture Zone: a recorder of continents drifts and kinematic changes. Tectonophysics 823, 229188. https://doi.org/10.1016/j.tecto.2021.229188.
Roche, V., Leroy, S., Revillon, S., Guillocheau, F., Ruffet, G., Vétel, W., 2022. Gondwana Break-Up Controlled by Tectonic Inheritance and Mantle Plume Activity: Insights from Natal Rift Development (South Mozambique, Africa). Terra Nova. https://doi.org/10.1111/ter.12590.
Rodgers, K.A., Chisholm, J.E., Davis, R.J., Nelson, C.S., 1977. Motukoreaite, a new hydrated carbonate, sulphate, and hydroxide of Mg and Al from Auckland, New Zealand. Mineral. Mag. 41 (319), 389–390.
Roeder, P.L., Rf, Emslie, 1970. Olivine-liquid equilibrium. Contrib. Mineral. Petrol. 29, 275–289.
Saria, E., Calais, E., Stamps, D.S., et al., 2014. Present-day kinematics of the East African Rift. J. Geophys. Res. Solid Earth 119, 3584–3600. https://doi.org/10.1002/2013JB010901.
Senkans, A., Leroy, S., d'Acremont, E., Castilla, R., Despinois, F., 2019. Polyphase rifting and break-up of the Central Mozambique margin. Mar. Pet. Geol. 100, 412–433. https://doi.org/10.1016/j.marpetgeo.2018.10.035.
Sparks, R.S.J., Annen, C., Blundy, J.D., et al., 2019. Formation and dynamics of magma reservoirs. Philos Trans R Soc A 377, 20180019.
Späth, A., Le, Roex A.P., Duncan, R.A., 1996. The geochemistry of lavas from the Comores Archipelago, Western Indian Ocean: petrogenesis and mantle source region characteristics. J. Petrol. 37, 961–991. https://doi.org/10.1093/petrology/37.4.961.
Strong, D.F., 1972. Petrology of the island of Moheli, western Indian Ocean. Geol. Soc. Am. Bull. 83, 389–406. https://doi.org/10.1130/0016-7606(1972)83[389:POTIOM]2.0.CO;2.
Thinon, I., Lemoine, A., Leroy, S., Paquet, F., Berthod, C., Zaragosi, S., Famin, V., Feuillet, N., Boymond, P., Masquelet, C., Mercury, N., Rusquet, A., Scalabrin, C., Van der Woerd, J., Bernard, J., Bignon, J., Clouard, V., Doubre, C., Jacques, E., Jorry, S. J., Rolandone, F., Chamot-Rooke, N., Delescluse, M., Franke, D., Watremez, L., Bachelery, P., Michon, L., Sauter, D., Bujan, S., Canva, A., Dassie, E., Roche, V., Ali, S., Sitti Allaouia, A.H., Deplus, C., Rad, S., Sadeski, L., 2022. Volcanism and tectonics unveiled in the Comoros Archipelago between Africa and Madagascar. Comptes Rendus. G´eosci. 354, 1–28. https://doi.org/10.5802/crgeos.159.
Thompson, R.N., Flower, M.F.J., 1971. One-atmosphere melting and crystallization relations of lavas from Anjouan, Comores Archipelago, Western Indian Ocean. Earth Planet. Sci. Lett. 12 (1), 97–107. https://doi.org/10.1016/0012-821X(71)90060-4.

Tsekhmistrenko, M., Sigloch, K., Hosseini, K., Barruol, G., 2021. A tree of Indo-African mantle plumes imaged by seismic tomography. Nat. Geosci. 14, 612–619. https://doi.org/10.1038/s41561-021-00762-9.

Verma, S.P., 1981. Seawater alteration effects on 87Sr86Sr, K, Rb, Cs, Ba and Sr in oceanic igneous rocks. Chem. Geol. 34 (1–2), 81–89.

Vormann, M., Jokat, W., 2021. The crustal structure of the Kerimbas Basin across the offshore branch of the East African Rift System. Geophys. J. Int. 226 (3), 2073–2102. https://doi.org/10.1093/gji/ggab194.

Vozniak, A.A., Kopylova, M.G., Nosova, A.A., Sazonova, L.V., Lebedeva, N.M., Stifeeva, M.V., 2023. Compositional evolution of igneous garnets: calcic garnets from alkaline rocks of Terskiy Coast (Kola Alkaline Carbonatite Province). Mineral. Petrol. 117 (3), 553–571.

Watremez, L., Leroy, S., d'Acremont, E., Roche, V., Evain, M., Leprêtre, A., Moulin, M., 2021. The Limpopo Magma-Rich Transform margin, South Mozambique: 1. Insights from Deep-Structure Seismic Imaging. Tectonics 40 (12), e2021TC006915. https://doi.org/10.1029/2021TC006914.

Welsch, B., Hammer, J., Hellebrand, E., 2014. Phosphorus zoning reveals dendritic architecture of olivine. Geology 42 (10), 867–870. https://doi.org/10.1130/G35691.1.

Wiles, E., Watkeys, M., Jokat, W., 2020. Surface expression of microplate boundary kinematics: an isolated abyssal hill in the Mozambique Channel. J. Afr. Earth Sci. 168, 103830. https://doi.org/10.1016/j.jafrearsci.2020.103830.

Zeng, G., Chen, L.H., Yu, X., Liu, J.Q., Xu, X.S., Erdmann, S., 2017. Magma-magma interaction in the mantle beneath eastern China. J. Geophys. Res. Solid Earth 122 (4), 2763–2779. https://doi.org/10.1002/2017JB014023.